JOURNAL OF GEOPHYSICAL RESEARCH, VOL. 115, E07011, doi:10.1029/2009JE003496, 2010

Inverted fluvial features in the Aeolis/Zephyria Plana region, Mars: Formation mechanism and initial paleodischarge estimates

Devon M. Burr,[1] Rebecca M. E. Williams,[2] Kimberly D. Wendell,[3,4] Matthew Chojnacki,[1] and Joshua P. Emery[1]

Received 25 August 2009; revised 22 February 2010; accepted 24 March 2010; published 27 July 2010.

[1] A subset of the sinuous ridges (SRs) in the Aeolis/Zephyria Plana (AZP) region of Mars has been previously hypothesized to be inverted fluvial features, although the precise induration and erosion mechanisms were not specified. Morphological observations and thermal inertia data presented here support this hypothesis. A variety of mechanisms can cause inversion, and identification of the specific events that lead to fluvial SR formation can provide insights into the sedimentological, geochemical, and climatic processes of the region. Reconnaissance of two terrestrial lava-capped ridges suggests some criteria that may be used to identify inverted fluvial features formed by lava infill on Mars, but these criteria are not satisfied by the majority of the AZP fluvial SRs. Armoring also appears inconsistent with terrestrial analogs. Layering and surface textures of fluvial SRs indicate that the most likely induration mechanism was geochemical cementation of fluvial sediments, and that the primary erosional mechanism that exposed the fluvial SRs was aeolian abrasion. This analysis of formation mechanism provides a foundation for estimating paleodischarge using an empirical form-discharge approach, to which we have applied scaling, for Martian gravity. For those fluvial SRs meeting a set of criteria for accurate paleodischarge estimates, paleodischarge values generally range between 10^1 and 10^3 m^3 s^{-1}. The largest of these initial estimates are comparable to paleodischarge estimates for some late-stage Noachian fluvial channels on Mars, and provide a constraint on the atmospheric conditions at this equatorial location during the late Hesperian to early Amazonian time frame.

Citation: Burr, D. M., R. M. E. Williams, K. D. Wendell, M. Chojnacki, and J. P. Emery (2010), Inverted fluvial features in the Aeolis/Zephyria Plana region, Mars: Formation mechanism and initial paleodischarge estimates, *J. Geophys. Res.*, *115*, E07011, doi:10.1029/2009JE003496.

1. Introduction

[2] At the equator of Mars, between the Aeolis and Zephyri Plana (AZP), is an extensive population of sinuous ridges (SRs) [*Burr et al.*, 2006b, 2009; *Pain et al.*, 2007], the largest and most densely packed cluster of such features yet documented on Mars. This population is located at the global dichotomy boundary and concentrated in the two western-most lobes of the Medusae Fossae Formation (MFF) (Figure 1), which are dated to have formed during the Hesperian to early Amazonia epochs (see references and discussion from *Burr et al.* [2009], also *Kerber and Head* [2010]). The large majority of these SRs are located around the edges of the highstanding MFF lobes and trend from high to low elevations. They have morphologies consistent with formation by flowing water [*Burr et al.*, 2009] and are inferred to be inverted fluvial landforms, although a detailed formation mechanism was not previously determined. The investigations presented herein build on prior work to assess the formation mechanism for these fluvial SRs and provide initial estimates of their paleodischarges. The results of the work have bearing on the equatorial climatic conditions in the late Hesperian to early Amazonian.

[3] The runoff that formed these fluvial SRs was inferred to have come from precipitation falling on the MFF during its emplacement [*Burr et al.*, 2009]. Some of these SRs have high sinuosities (up to 2.4), implying long-lived flow. Thus, paleodischarge estimates provide constraints on the long-term atmospheric conditions during SR formation and their effect on surface morphology and sediment transport within the western MFF. Paleodischarges have been previously estimated for inverted [*Moore et al.*, 2003] and normal negative-relief fluvial features on Mars [*Irwin et al.*, 2005; *Fassett and Head*, 2005] using form-discharge relationships. The accuracy of paleodischarge estimation based on relationships between fluvial form and discharge depends significantly on feature width and wavelength preservation, which differ with differing inversion mechanisms.

[1]Earth and Planetary Science Department, University of Tennessee Knoxville, Knoxville, Tennessee, USA.
[2]Planetary Science Institute, Tucson, Arizona, USA.
[3]Formerly at Department of Earth Sciences, Montana State University, Bozeman, Montana, USA.
[4]Bozeman, Montana, USA.

0148-0227/10/2009JE003496

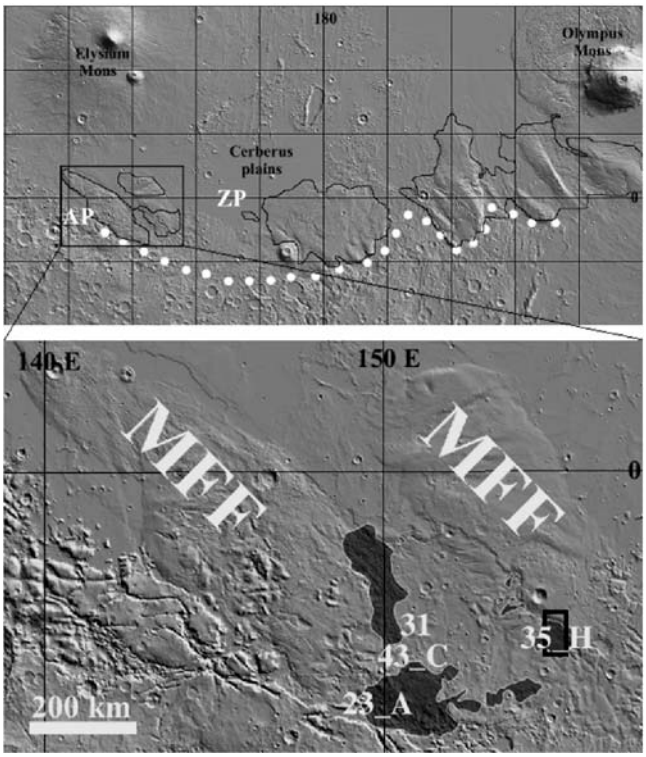

Figure 1. Mars Orbiter Laser Altimeter (MOLA) shaded relief topography with artificial illumination from the upper right. (top) Regional context with a 10° grid and significant landmarks labeled in black. The Medusae Fossae Formation is outlined in black, and the global dichotomy is shown in white dots. AP = Aeolis Planum, ZP = Zephyria Planum. (bottom) The two western-most lobes of the Medusae Fossae formation (MFF), as labeled in white. The black rectangle shows the approximate location of Figure 2a (Area35_H). White labels indicate the approximate locations of Figure 3b (23_A), Figure 3c (Area31), and Figure 8 (Area43_C). Areas with particularly high-densities of SRs are shaded dark gray, although SRs are scattered throughout the region. For a fuller mapping of individual SRs derived from THEMIS visible wavelength images, see *Burr et al.* [2009] (Figure 9).

[4] The present work provides an analysis of the likely inversion mechanism for the fluvial SRs in the AZP from morphologic and thermal inertia investigations, followed by initial estimates based on form-discharge relationships for paleodischarge. The work begins with a brief review of the possible mechanisms for feature inversion and a summary of the fluvial SR morphologies. This review is followed by a description of our data and methods for the morphologic analyses, thermal inertia derivations, and paleodischarge estimates. Following the methods section, we present our results for each of these three investigations. Finally, we discuss implications of this work.

2. Background

2.1. Fluvial Inversion on Earth and Mars

[5] Features are inverted through a process of differential erosion that occurs when they develop greater resistance than the surrounding terrain. For fluvial features, this development may result from infill of the channel and possibly the surrounding alluvial valley by a resistant material; on Earth, this material is commonly lava. As a second possibility, induration may result from cementation of the fluvial sediments by various natural geochemical cements, whose formation commonly requires the presence of water. Inversion of alluvial valleys may occur through armoring of the valley floors by large-grained sediments, which increase resistance to erosion.

[6] Following one of these induration mechanisms, wide-spread erosion removes the less resistant material surrounding the paleofluvial features, leaving the features in positive relief. On Earth, wide-spread sedimentary erosion is commonly a result of enhanced entrainment during runoff. Such enhanced entrainment may be caused by increased precipitation associated with climate change or by a relative decrease in base level associated with either tectonic uplift or base level lowering. During the putatively warm and wet Noachian Period, fluvial entrainment may have been the primary mechanism for wide-spread erosion [e.g., *Carr*, 1996]. Within the last few billion years of Mars' history, in the inferred absence of a global hydrological cycle, wide-spread erosion was likely caused by aeolian abrasion [e.g., *Greeley et al.*, 2002]. See *Pain and Ollier* [1995] for a review of fluvial channel inversion on Earth, and *Pain et al.* [2007] for an overview of landscape inversion on Mars.

2.2. Fluvial SR Context and Morphologies

[7] Although the origin of the MFF is still uncertain, available data are consistent with high porosity volcanoclastic sediments [*Bradley et al.*, 2002; *Hynek et al.*, 2003; *Mandt et al.*, 2008; *Carter et al.*, 2009], which would provide a friable and easily eroded lithologic unit. Regardless of its origin, the MFF landscape has been heavily eroded, as indicated by the pervasive yardangs [*Ward*, 1979; *Scott and Tanaka*, 1982; *Wells and Zimbelman*, 1997; *Mandt et al.*, 2008]. Thus, the lithologic context for the AZP SRs is conducive to the wide-spread erosion that is necessary for landscape inversion.

[8] The fluvial SRs in the AZP region give specific contextual and morphologic indications of having developed through greater resistance to erosion than the surrounding terrain [*Burr et al.*, 2009]. The SRs tend to cluster around and extend outward from the edges of the two MFF lobes, where they appear to have been exposed through backwasting and/or downwearing of MFF material. In some cases, SRs transition from ridges into disjointed, often flat-topped knobs, inferred to be a result of advanced aeolian erosion of an indurated material (Figures 2a and 3c). Although not all SRs are highstanding (e.g., Figure 3b), most flat SRs have steep sides up to several tens of meters high, indicative of the cohesion or strength of the material. This inference from morphology and context that SR formation has involved erosion is consistent with previous publications that have inferred extensive erosion in this region [*Irwin et al.*, 2004; *Mandt et al.*, 2008, 2009].

[9] In addition to being inverted, many of the sinuous ridges (e.g., those that extend outward from the edges of the MFF) are exhumed landforms which have been exposed through erosion of the MFF. In these cases, the former drainage basins (or watershed catchments) remain buried. In other cases, evidence of the former drainage basins has been

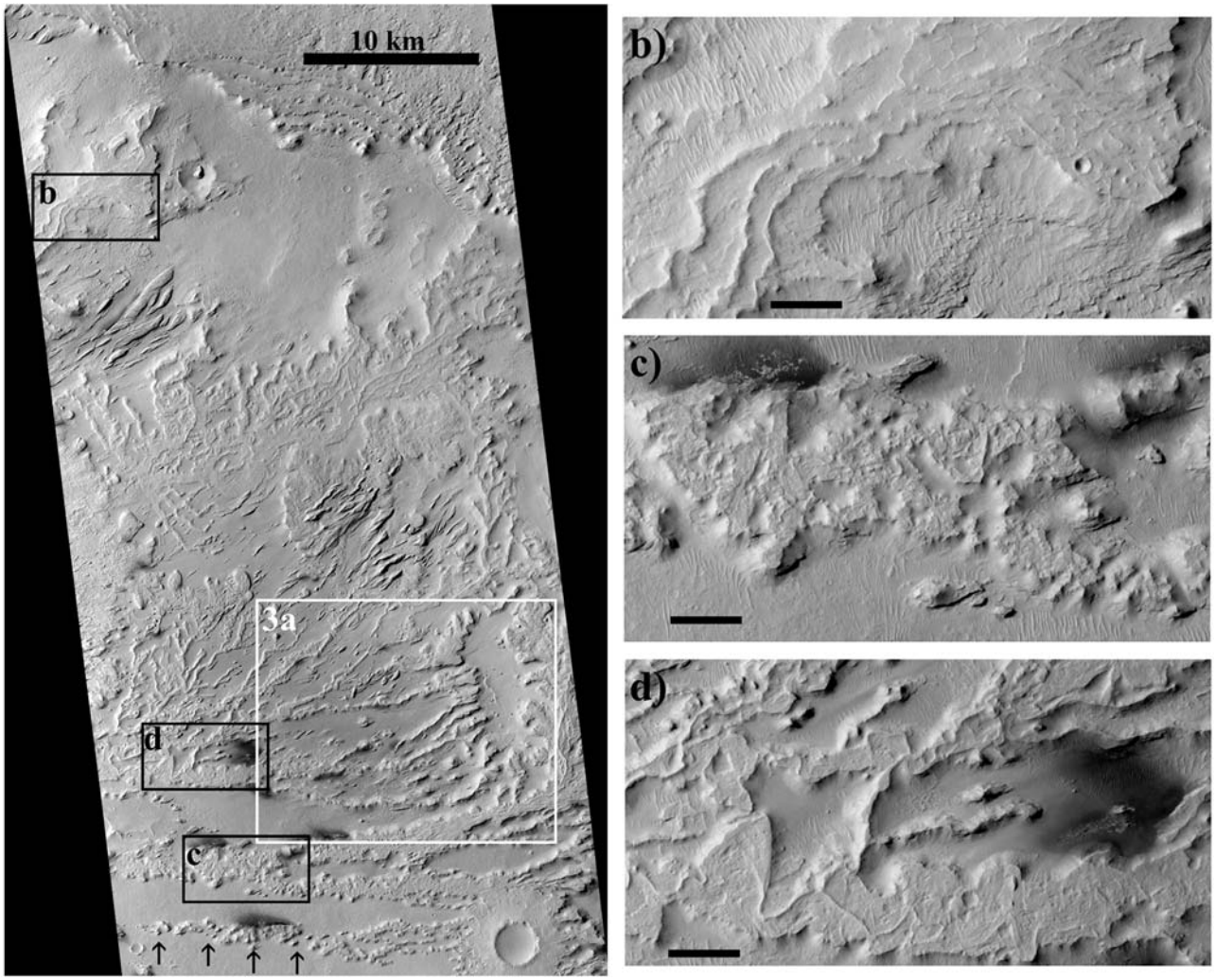

Figure 2. (a) Portion of CTX image P02_001870_1748_XN_05S204W showing examples of the various morphologies and complex stratigraphy exhibited by SRs in the AZP region. Black boxes indicate the locations of Figures 2b–2d. Black arrows at lower left point to an example of an SR transitioning into disjointed knobs. White box shows the approximate location of Figure 3a. In all images, illumination is from the west (left). For Figures 2b–2d, the black scale bars are each 1 km. (b) Example of a branching thin SR network (Area35_A) [*Burr et al.*, 2009, Table 1]. (c) Example of a branching flat SR (Area35_E) [*Burr et al.*, 2009, Table 1]. (d) Examples of two multilevel SRs (Area35_F) [*Burr et al.*, 2009, Table 1].

largely eroded away. Gridded MOLA topography has allowed for reconstruction of the general source area for one SR network [*Burr et al.*, 2009]. Ongoing inspection of new high-resolution images may yield additional clues as to the source areas for the fluvial SRs.

[10] The AZP SRs have been grouped into five morphological classes, based on an assessment of shape and relative size. This assessment was derived largely from SR appearance in visible wavelength images from the Thermal Emission Imaging Spectrometer (THEMIS) [*Christensen et al.*, 2003], which provided sufficient resolution to see morphological attributes and enough coverage to determine local context. Scattered images from the Mars Orbiter Camera (MOC) [*Malin and Edgett*, 2001] and High Resolution Imaging Science Experiment (HiRISE) [*McEwen et al.*, 2007] were used where possible to verify features from THEMIS images.

[11] Three of the five morphologic classes – which together include over 80% of the tabulated SRs – are interpreted as inverted fluvial features of various types [*Burr et al.*, 2009]. Each of the three fluvial SR types is distinctive in size and appearance (Figure 2a). Thin SRs (Figure 2b; see also Figures 3a, 3c, and 8a) display fairly constant widths of order tens of meters with distance along the ridge and are interpreted as inverted fluvial channels. Flat SRs (Figure 2c; see also Figures 3a and 3b), generally a few hundred of meters to greater than a kilometer in width, have broadly flat-looking upper surfaces, sometimes with sub-parallel arcuate lineations; these are interpreted as the meander belts of inverted floodplains. Multilevel SRs (Figure 2d) show superjacent thin SRs lying on subjacent flat SRs, and are interpreted as inverted fluvial channels superposed on inverted floodplains. *Burr et al.* [2009] provide an initial tabulation from THEMIS data of SR location, approximate

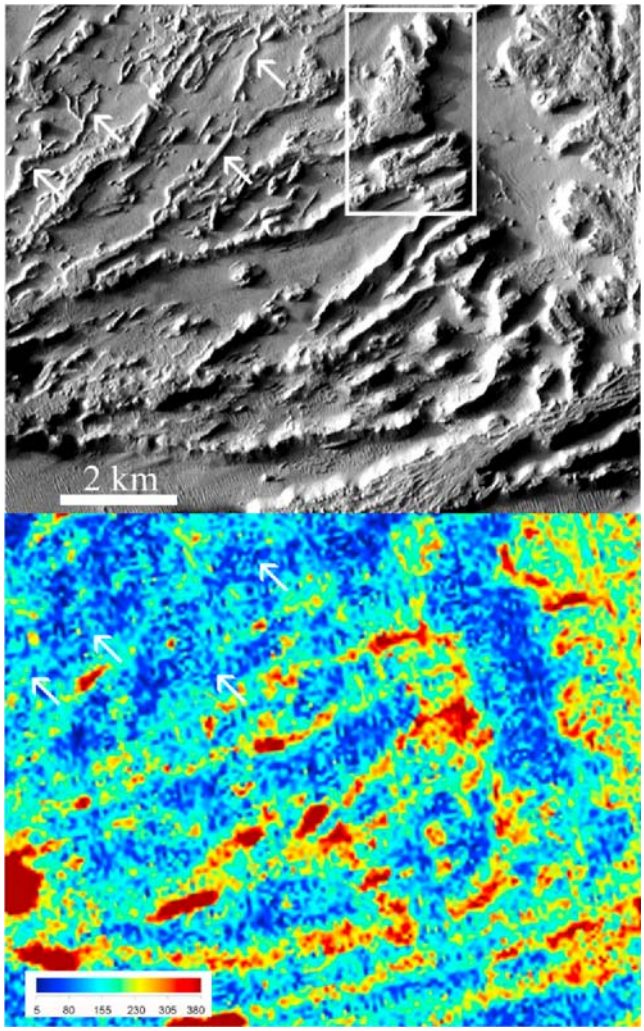

Figure 3a. (top) Portion of CTX image P02_001870_1748_XN_05S204W and (bottom) thermal inertia image from THEMIS night IR image I3132761060 showing part of a branching multilevel SR network (Area35_H) [*Burr et al.*, 2009, Table 1]. The majority of the branches have thermal inertia values that are up to a few hundred tiu higher than the surrounding terrain. White arrows in the upper left corners of both images point out thin SRs that are apparent in the visible wavelength image but not in the thermal inertia image. The white box highlights an unusual example of terminal widening, which may be attributable to lava-infill. The length scale bar applies to both images. The units on the color bar scale range from 5 tiu to 380 tiu by 75 tiu per mark, where tiu (thermal inertia units) are J m^{-2} K^{-1} $s^{-1/2}$. Illumination for the visible wavelength image is from the west (left).

elevation, and morphological class; SR identifiers used in this work are from that table.

3. Methods

3.1. Morphological Analysis

[12] Along with new THEMIS and MOC visible wavelength images, data from the Context Camera (CTX) [*Malin et al.*, 2007] and HiRISE reveal additional detail. In this work, we use available CTX and HiRISE images to assess fluvial SR morphologies at a range of scales. In addition, we conducted field investigations of some possible terrestrial analogs to derive morphologic criteria for determining SR formation mechanism.

3.2. Thermal Inertia Derivations

[13] Thermal inertia is a function of thermal conductivity, density, and specific heat capacity [e.g., *Kieffer et al.*, 1977; *Mellon et al.*, 2000]. For materials of the same composition, thermal inertia increases with grain size, denser packing, and/or reduced pore space [e.g., *Kieffer et al.*, 1977; *Mellon et al.*, 2000; *Putzig and Mellon*, 2007]. As explained

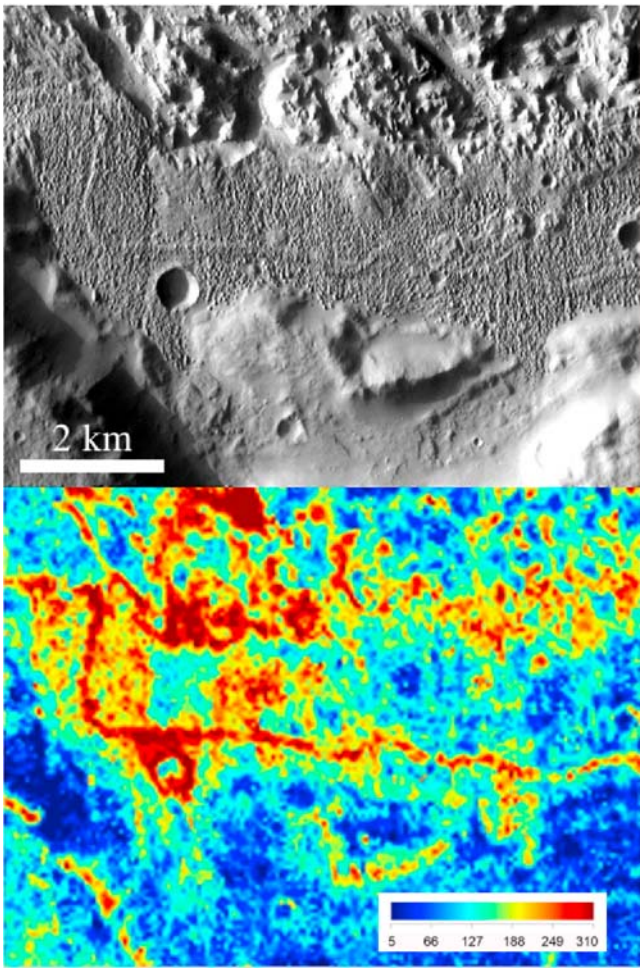

Figure 3b. (top) Portion of THEMIS visible wavelength image V05251001 and (bottom) thermal inertia image from THEMIS night IR image I08078012 showing an isolated flat SR (Area23_A) [*Burr et al.*, 2009, Table 1], oriented east–west across the image. Although the inferred SR is unexhumed or only slightly exhumed from the surroundings, it still displays a higher thermal inertia than the surrounding terrain. The length scale bar applies to both images. The units on the color bar scale range from 5 tiu to 310 tiu by 51 tiu per mark. Illumination for the visible wavelength image is from the west (left).

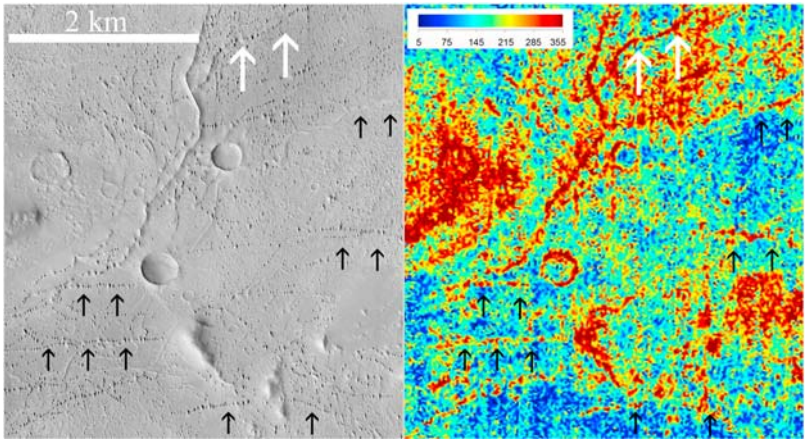

Figure 3c. (left) Portion of CTX visible wavelength image P08_004336_1742_XI_05S208W and (right) thermal inertia from THEMIS night IR image I32337007, showing multiple thin SRs or erosional relicts of SRs (Area31) [*Burr et al.*, 2009, Table 1]. The best-preserved SR is oriented north–south in the upper center of the image, with an eastern branch that has transitioned into an alignment of small knobs but which has an equally significant thermal inertia signature (two white arrows). Other SR relicts that are visible in thermal inertia data are pointed out by black arrows on both images. The length scale bar applies to both images. The units on the color bar scale range from 5 tiu to 355 tiu by 70 tiu per mark. Illumination for the visible wavelength image is from the west (left).

by *Christensen* [1982], an interpretation of thermal inertia values cannot be uniquely assigned. For example, the thermal inertia of bedrock lava may be reduced by vesicularity [*Zimbelman*, 1986] whereas the thermal inertia of sediments may be increased by cementation [*Mellon et al.*, 2000], such that variation in these factors may produce similar thermal inertia values for different material. The three mechanisms that can cause increased resistance in channels - chemical cementation, armoring, and lava infill - would all serve to increase the thermal inertia values of the channels. Thus, elevated thermal inertia values, as derived below, provide support for the interpretation based on morphological and contextual data of SR formation through inversion.

[14] Nighttime infrared (IR) images are more sensitive to the thermophysical properties of the surface materials, whereas daytime IR images are more responsive to insolation [*Christensen et al.*, 2003]. For this work, we examined THEMIS nighttime (IR) images (res. 100 m px^{-1}) over all interpreted fluvial SRs to identify SRs with elevated brightness temperatures, which would in turn indicate elevated thermal inertia values. For those SRs that were apparent in nighttime THEMIS IR images, thermal inertia images were created with in-house ENVI © routines utilizing lookup tables generated by the model of *Putzig and Mellon* [2007]. In this method, the corrected radiance from band 9 (centered at 12.6 μm) is fitted to a Planck curve to derive nighttime brightness temperature. This brightness temperature is then correlated with the *Putzig and Mellon* [2007] lookup table for the best fitting season, time of day, latitude, surface pressure, dust opacity and albedo to arrive at a optimal thermal inertia (see *Fergason et al.* [2006] and *Putzig and Mellon* [2007] for a full description). These thermal inertia images were then queried manually to estimate the maximum range of values for the SRs and for the average of the surrounding terrain.

3.3. Paleodischarge Estimates

3.3.1. Approach

[15] Paleodischarge can be estimated directly using empirical relationships between paleochannel dimensions and discharge that have been derived for terrestrial rivers and then scaled for Martian gravity. As the thin SRs are inferred paleochannels, we adopt this so-called form-discharge (or macro-scale or hydrologic) approach here for application to thin SRs. Paleodischarges have been previously estimated for both positive-relief (inverted) [*Moore et al.*, 2003] and negative-relief (normal) fluvial features on Mars [*Irwin et al.*, 2005; *Fassett and Head*, 2005] using this form-discharge approach.

[16] Alternatively, various workers have determined methods for estimating discharge by considering the driving forces to mobilize sediment in a channel. These relationships depend on the grain size distribution, channel slope and channel shape (width and water depth), and have been applied to inverted terrestrial paleochannels by *Williams et al.* [2009]. However, this region of Mars is dusty [*Ruff and Christensen*, 2002], obscuring MFF grain size data from remote observation. Recent analyses of the MFF suggest that it is a pyroclastic flow deposit [*Mandt et al.*, 2008; *Carter et al.*, 2009; see also *Scott and Tanaka*, 1982], for which in terrestrial examples grain size may vary by an order of magnitude [e.g., *Sparks*, 1976]. And slope information in this equatorial region is low in resolution, although topography may be derived from stereo CTX and HiRISE images. Because of these current data limitations, we do not use these micro-scale or hydraulic methods for estimating paleodischarge values.

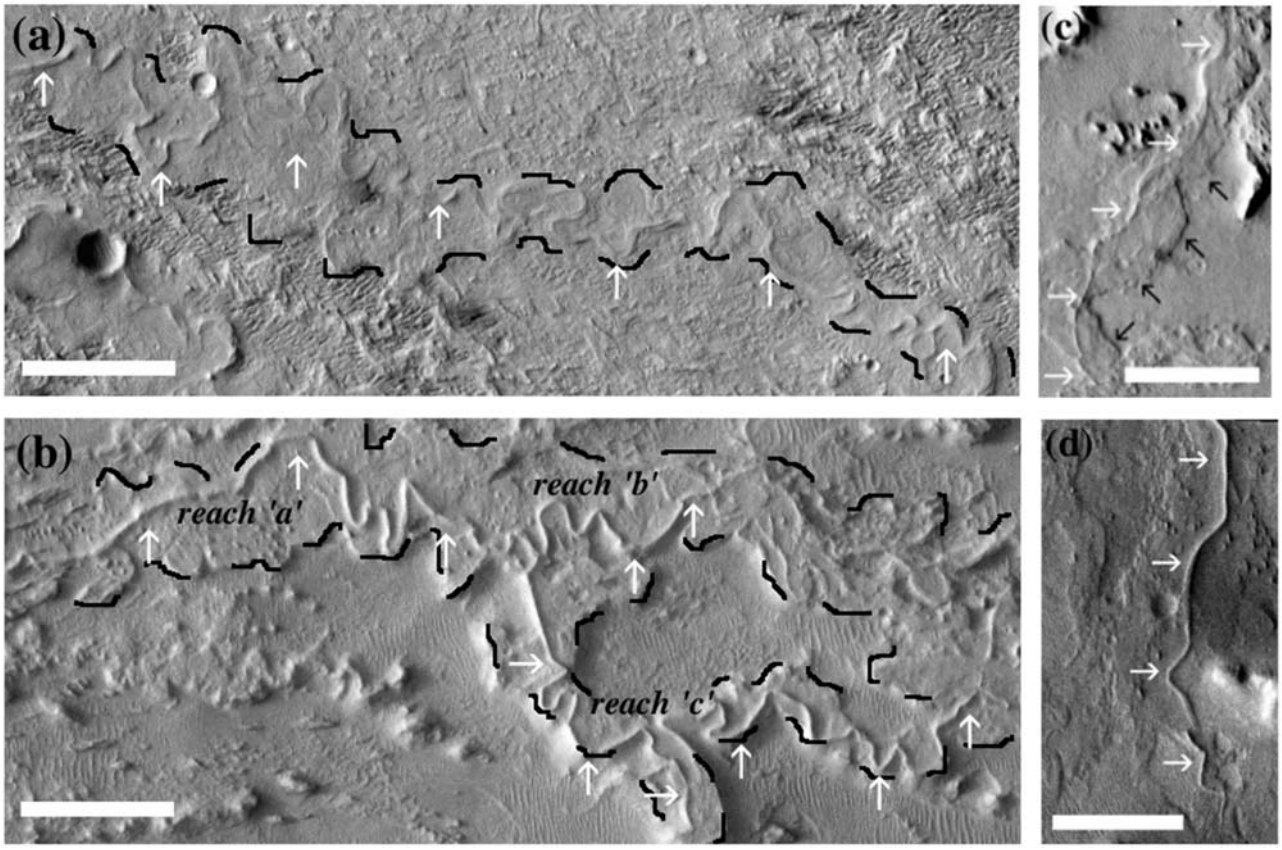

Figure 4. Portions of THEMIS visible wavelength images showing the reaches of the SRs (white arrows) for which wavelength-to-width ratios were within ±25% of the terrestrial range of 10–14. In all images, illumination is from the left (west), and the scale bar is 2 km. (a) Portion of image V19254001 showing the thin SR 34C.a, which forms the superjacent level of a multilevel SR. The subjacent flat SR is outlined with black dashes. In some locations, the edge of the subjacent flat SR and superjacent thin SR are coincident. (b) Portion of image V05875001 showing the thin SRs 35E.a. 35E.b, and 35E.c (labeled in black). These thin SRs form the superjacent level of a multilevel SR network. The subjacent flat SR is outlined with black dashes, which in some locations, is co-located with the edge of the superjacent thin SR. This SR also illustrates the coincidence between the two levels of a multilevel SR, shown, for example, where the meander loop at the bottom of the image (beneath "reach 'c'"), though distinctly elongated, remains coincident with the underlying flat SR. (c) Portion of image V18031002 showing thin SR 39C.a. Despite its appearance in this image, this SR is not classified as multilevel, as a larger view shows that the seemingly subjacent flat SR seen here (black arrows) is not widely coincident with the thin SR (white arrows). (d) Portion of image V14986002 showing thin SR 41A.a.

[17] The dimensions of meander belts are not directly related to discharge and so require additional analysis. Thus, discharges for the flat SRs are not presented here.

3.3.2. Assessment of Feature Preservation

[18] Using the form-discharge approach, paleodischarge may be estimated both from channel width and from meander wavelength. Error is introduced into such paleoflow discharge estimates if these measured parameters do not accurately reflect the paleoflow conditions. The widespread yardangs of the MFF indicate that the unit has been heavily eroded by aeolian abrasion [*Ward*, 1979; *Wells and Zimbelman*, 1997; *Mandt et al.*, 2008]. However, the degree of erosion may be evaluated through morphological study.

[19] Inverted paleochannels in northeastern Utah, United States, illustrate differences in the preservation morphology along course depending on the type of channel deposit. Point-bar deposits located on the inside of paleochannel inflections generally eroded to a rounded cross-sectional shape with variable width. In contrast, segments of channel fill have high-angle sides with relatively constant width [*Harris*, 1980; *Williams et al.*, 2007, 2009]. These channel-fill segments are inferred to represent preservation of the original channel width. Thus, high-angle sides and uniform widths suggest the locations of meander crossings and provide a qualitative metric for candidate reaches that best provide accurate paleoflow width data.

[20] For freely meandering river channels, wavelength provides another parameter from which to estimate paleodischarge. Circumstantial observations suggest that the SRs were freely meandering. The hypothesized fine-grained

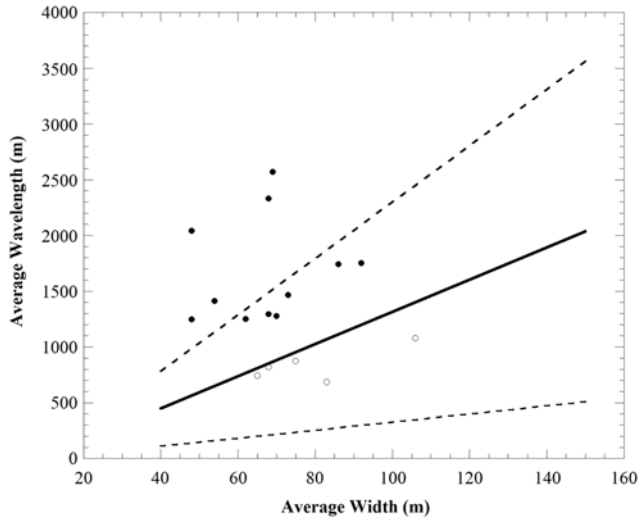

Figure 5. Plot of average wavelength versus average width values for the 16 sinuous ridges within the study region for which paleodischarge values were calculated. Open circles signify SRs whose wavelength-to-width ratio is less than 25% different than the terrestrial value and correspond to the examples in Table 1 without bolding; solid circles signify SRs whose wavelength-to-width ratio is more than 25% different than the terrestrial value and correspond to the bolded portion of Table 1. For comparison, a typical terrestrial correlation of width and wavelength values is plotted (solid line) for meandering streams with sinuosity ≥1.2 and an error envelope (dashed line) of 0.219 log units (*Williams* [1986], updated by *Williams* [1988]). For those Martian examples that fall outside the terrestrial error envelope, the assumption that wavelength is better preserved than width implies that width would have to increase (shift to the right on the plot) to fit within the terrestrial range. This finding is consistent with and illustrative that width has been poorly preserved for the majority of these SRs.

volcaniclastic sediments comprising the MFF are a reasonable substrate in which meandering would occur. And the surface texture of some flat SRs, which show arcuate, semiconcentric lineations, are hypothesized to be paleoscroll bars (point bar ridges) produced during meandering [*Burr et al.*, 2009]. These inferred scroll bars are not visible on all flat SRs, nor is evidence of meandering discernable on the smaller-scale thin SRs in the Mars Orbiter Camera (MOC) or available HiRISE images. However, the close planform coincidence in multilevel SRs between the subjacent flat SRs and the superjacent thin SRs (e.g., Figure 2d) provides inferential evidence that the two levels formed through similar morphological processes, including meandering. The planform morphology of some thin SRs (e.g., Figure 4b) is similar to irregular or tortuous meanders [see, e.g., *Knighton*, 1998, Figure 5.18], which may form in the presence of strong banks. However, tortuous meanders are not diagnostic of confined meandering, and are not common among those SRs for which paleodischarge was estimated (Figures 4a, 4c, and 4d). Thus, some ambiguity exists on the question of whether (or which) thin SRs meandered freely, but evidence available to date supports an hypothesis of free meandering.

[21] While wavelength measurements can be used for paleodischarge estimation, wavelength also provides a quantitative criterion with which to assess width erosion. Meander wavelength is not significantly altered by erosion, and thus serves as a more unambiguous parameter than width regarding paleoflow conditions. Terrestrial meandering channels have average wavelength-to-width ratios of 10 to 14 [*Knighton*, 1998, p. 215]. Because width may be affected by erosion whereas meander wavelength is not, inverted paleochannels whose widths have been eroded will have higher than normal wavelength-to-width ratios.

[22] Thus, for this work, we assume that the thin SRs meandered freely, so that the wavelength-to-width ratio provides some indication of erosion. As a criterion for paleodischarge calculation, we used wavelength-to-width ratios of ~8 to 16 (approximately 25% below and 25% above the range of terrestrial values). However, for completeness, we have included thin SRs with wavelength-to-width values greater than ~16 if they fulfilled all other criteria. A plot of the wavelength and width data is shown in Figure 5.

3.3.3. Types of Discharge Calculations

[23] In view of the large uncertainties in estimating paleodischarge (discussed in Appendix A), the goal of this work is to estimate an order of magnitude value for the average discharges and the channel-forming flood discharges in these Martian fluvial landforms.

[24] The particular form-discharge relationships used in this work were derived from empirical studies for rivers in the United States (summarized by *Williams* [1988]). Both width and wavelength measurements were used to provide estimates for average daily discharge, or 'the steady discharge occurring continuously for an average day of flow' [*Williams*, 1988]. On Earth, the average discharge is useful in representing the amount of drainage basin precipitation that feeds the river, and so provides a linkage to climate. It is also the statistical discharge cited most frequently in terrestrial studies probably because of ease of estimation [*Williams*, 1988].

[25] In addition, both width and wavelength were used to provide estimates for the channel-forming flood discharge, sometimes referred to as the mean annual peak flow, 'mean annual flood,' or dominant flood, and generally supposed to have a recurrence interval of 1–2 years [*Williams*, 1988; *Knighton*, 1998]. Like the average discharge, this flood discharge is a statistical value determined from many measurements at a single gauging site. Floods of this magnitude appear to control alluvial channel dimensions, but limitations to this relationship are noted [*Knighton*, 1998, pp.162–167]. The 2-year flood discharge has been cited in previous works related to Mars fluvial estimates [*Irwin et al.*, 2005; *Williams et al.*, 2009], whereas the similar 1.5-year flood has been used as the channel-forming discharge by other terrestrial workers.

[26] Our use of the 2-year and 1.5-year floods does not imply any particular recurrence interval on Mars. We use these terms only to denote channel-forming flood discharges. The four equations used in this work – based on width and wavelength and used for the average daily

discharge and the channel-forming flood discharge – are discussed in Appendix A.

3.3.4. Scaling for Martian Gravity

[27] Gravity is the driving force in fluvial flow. Thus, empirical terrestrial relationships used for estimating Martian paleodischarge are commonly scaled for Martian gravity [e.g., *Komar*, 1980; *Wilson et al.*, 2004; *Moore et al.*, 2003; *Irwin et al.*, 2005, 2008]. Scaling empirical relationships is an uncertain endeavor, however, because, although the effect of gravity on sediment transport may be quantified [*Kleinhans*, 2005; *Burr et al.*, 2006a], the effect of gravity on the empirical relationships is unknown. Acknowledging this uncertainty, we have scaled our paleodischarge results for the lower gravity on Mars, in conformity with commonly accepted practices. However, if the scaling for gravity is superfluous when using empirical morphometric relationships, then the paleodischarge estimates presented in Table 1, which include scaling for the low gravity on Mars, likely underestimate the true paleodischarge values.

[28] Discharge is given by the continuity equation, in which discharge in units of length cubed per time is the product of flow depth, flow width, and flow velocity. In estimating extraterrestrial discharges from flow dimensions, the Darcy-Weisbach equation is considered most appropriate for accommodating the difference in gravity [*Wilson et al.*, 2004]. Setting the continuity equation equal to the Darcy-Weisbach equation gives the expression

$$Q = HWV = HW\left(\sqrt{8HgS}\Big/\sqrt{f}\right)^{0.5}, \quad (1)$$

where Q is the discharge ($m^3\ s^{-1}$), H is the flow depth (m), W is the flow width (m), V is the flow velocity ($m\ s^{-1}$), g is the gravitational acceleration ($m\ s^{-2}$), S is the slope (dimensionless), and f is the Darcy-Weisbach friction factor (dimensionless). This expression, which assumes steady and uniform flow, shows that to convey a given discharge in a channel of given roughness (f) and slope (S) under a lower gravity regime (g), the flow width and/or depth must increase. Alternatively, for the same channel conditions of width, depth, slope, and roughness under lower gravity, discharge decreases.

[29] As stated above, for this study, the dimensions of interest for estimating paleodischarge are width, W, and meander wavelength, L_m (Appendix A). Width and meander wavelength show a power law relationship with an exponent of 1.03 [*Knighton*, 1998, Figure 1.2C]. Given this nearly linear relationship within the regime of interest, the scaling values for width were also used as the scaling values for wavelength.

[30] The approach used here for deriving these scaling values is first to determine the factor by which the width would have to increase under Martian gravity for a given discharge, and then to substitute that factor into the empirical equations (Appendix A) to determine the factor by which the discharge would decrease for a given channel (i.e., given width, depth, slope, and roughness). These factors may be derived in two ways, either by using dimensionless flow parameters or by manipulation of regression equations. See Appendix B for these two derivations. The scaling factors derived from the two approaches are identical for the daily discharge (equations (A1) and (A3)), and for the channel-forming flood discharges (equations (A2) and (A4)), they differ by ≤20%. These similar results, given by these two different approaches, suggest their accuracy. The scaling factors from both approaches are cited in Table 1 and are propagated through the error analysis (see section 3.3.6).

3.3.5. Data Collection

[31] THEMIS visible wavelength images (18 m/pix) provide sufficient resolution to distinguish SR morphology, as well as reasonable coverage of the region. Collection of data was a multistep process to ensure that the application of each equation to each SR was valid. In this process, all 52 thin SRs and all 27 superjacent thin SRs occurring as the upper level of multilevel SRs [*Burr et al.*, 2009, Table 1] were examined to search for possible valid applications. SRs used in this work are identified following the scheme used by *Burr et al.* [2009], in which each image or image mosaic was identified with a number and each SR network within that image or mosaic was identified with a letter. Here, a second lower case letter was appended to the identifier to designate an individual SR reach within the network.

[32] SRs were first assessed qualitatively for visibility and preservation. Sufficient shadowing was necessary to discern SR edges and satisfy the criteria for high angle sides, which for terrestrial examples from Utah, United States are inferred to represent well-preserved reaches of channel fill [*Williams et al.*, 2007, 2009]. SR continuity was also assessed in order to identify well-preserved examples. Because the estimates were to be based on meander wavelength as well as feature width, reaches having fewer than one complete wavelength were excluded from consideration.

[33] Each SR reach was then evaluated quantitatively with regard to its fitness for generating valid data. SRs for which width and/or wavelength fell outside the ranges specified for each of the terrestrial empirical equations (see Appendix A) were excluded from consideration. Because average meander wavelength was difficult to measure precisely for low sinuosity reaches, reaches with sinuosities of less than 1.1 were also excluded. In terrestrial studies, a minimum sinuosity of 1.5 is often used to define a meander, although this criterion is somewhat arbitrary [*Knighton*, 1998]. About one-half of our SRs have average sinuosities less than 1.5, and we have included these cases (down to a cutoff of 1.1) to provide a larger sample set.

[34] As discussed above, wavelength-to-width ratios were calculated as possible indicators of erosion. Only six of these SRs have ratio values that are low enough (i.e., less than ~16) to be indicative of *un*-eroded, meandering rivers, and paleodischarge estimates for these SRs are therefore considered to have the highest precision. As discussed above, paleodischarge values greater than ~16 were also included in Table 1 for completeness, but are distinguished from the other results with bold font. Paleodischarges for SRs for which wavelengths could not be measured due to low sinuosity or which do not satisfy other criteria for the macro-scale approach are not included.

[35] A total of 16 SR reaches met all of the criteria for providing reliable paleodischarge estimates. Width data were collected roughly every 0.5 to 2 km where illumination and/or shading could be used to discern SR edges. Wavelength data were collected where a full sinusoidal wave could be discerned and measured through three mid-points of the meander. The data for each SR were averaged and those

Table 1. Thin SR Reaches, Measured Parameters, and Estimated Discharge Values[a]

		Paleodischarge From Width						Paleodischarge From Wavelength					
				Scaled Q_ave (m^3 s^{-1}), Equation (A1)		Scaled Q_flood (m^3 s^{-1}), Equation (A2)				Scaled Q_ave (m^3 s^{-1}), Equation (A3)		Scaled Q_flood (m^3 s^{-1}), Equation (A4)	
ID	Morphology	Average Width (m)	Number of Data Points	Dim.Para (s.f. = 0.68)	Regress. Eqn. (s.f. = 0.68)	Dim. Para. (s.f. = 0.76)	Regress. Eqn. (s.f. = 0.62)	Average Wavelength (m)	Number of Data Points	Dim. Para. (s.f. = 0.62)	Regress. Eqn. (s.f. = 0.63)	Dim. Para. (s.f. = 0.71)	Regress. Eqn. (s.f. = 0.62)
	Thin	**69**	**10**	**26 (21)**	**26 (21)**	**253 (278)**	**206 (227)**	**2570**	**1**	**226 (59)**	**230 (60)**	**1393 (572)**	**1216 (499)**
1B	**Thin**	**86**	**12**	**37 (30)**	**37 (30)**	**330 (361)**	**269 (294)**	**1743**	**3**	**98 (52)**	**100 (53)**	**766 (404)**	**669 (353)**
19D	**Superjacent thin**	**73**	**8**	**28 (22)**	**28 (22)**	**269 (294)**	**219 (240)**	**1465**	**2**	**68 (29)**	**69 (30)**	**586 (281)**	**512 (245)**
34C.a	Superjacent thin	106	14	54 (44)	54 (44)	429 (472)	350 (385)	1079	7	35 (18)	36 (18)	366 (189)	319 (165)
35E.a	*Superjacent thin*	*83*	*16*	*35 (28)*	*35 (28)*	*315 (344)*	*257 (280)*	*685*	*2*	*13 (4)*	*13 (4)*	*182* (77)	*159* (67)
35E.b	*Superjacent thin*	*75*	*15*	*29 (23)*	*29 (23)*	*278 (304)*	*227 (248)*	*873*	*3*	*22 (21)*	*23 (21)*	*264* (201)	*231* (175)
35E.c	*Superjacent thin*	*65*	*8*	*23 (19)*	*23 (19)*	*235 (257)*	*192 (210)*	*740*	*1*	*16 (4)*	*16 (4)*	*205* (85)	*179* (75)
39C.a	**Thin**	**70**	**9**	**26 (22)**	**26 (22)**	**257 *(285)***	**210 (233)**	**1275**	**2**	**50 (16)**	**51 (16)**	**473 (203)**	**413 (177)**
39C.c	**Thin**	**68**	**13**	**25 (20)**	**25 (20)**	**247 (271)**	**202 (221)**	**1295**	**4**	**52 (18)**	**53 (19)**	**485 (216)**	**423 (188)**
40D.a	**Thin**	**92**	**10**	**42 (35)**	**42 (35)**	**359 (399)**	**293 (326)**	**1750**	**1**	**99 (26)**	**101 (27)**	**771 (317)**	**673 (277)**
40D.b	**Thin**	**62**	**11**	**21 (17)**	**21 (17)**	**221 (242)**	**180 (198)**	**1250**	**1**	**48 (13)**	**49 (13)**	**459 (189)**	**401 (165)**
41A.a	Thin	68	10	25 (20)	25 (20)	248 (273)	203 (223)	820	1	19 (5)	20 (5)	240 (100)	209 (87)
43A.a	**Superjacent thin**	**54**	**12**	**17 (14)**	**17 (14)**	**186 (205)**	**152 (167)**	**1412**	**5**	**62 (30)**	**63 (31)**	**554 (280)**	**484 (244)**
43C.h	**Thin**	**68**	**6**	**25 (20)**	**25 (20)**	**250 (274)**	**204 (224)**	**2330**	**2**	**183 (75)**	**186 (76)**	**1198 (560)**	**1046 (489)**
44B.a	**Thin**	**48**	**11**	**14 (11)**	**14 (11)**	**163 (180)**	**133 (147)**	**2040**	**2**	**138 (39)**	**140 (40)**	**976 (408)**	**852 (357)**
44D	**Thin**	**48**	**9**	**14 (11)**	**14 (11)**	**162 (176)**	**132 (144)**	**1246**	**2**	**48 (26)**	**48 (26)**	**457 (244)**	**399 (213)**

	Paleodischarge From Width				Paleodischarge From Wavelength			
	Scaled Q_ave (m^3 s^{-1}), Equation (A1)		Scaled Q_flood (m^3 s^{-1}), Equation (A2)		Scaled Q_ave (m^3 s^{-1}), Equation (A3)		Scaled Q_flood (m^3 s^{-1}), Equation (A4)	
Morphology	Dim.Para (s.f. = 0.68)	Regress. Eqn. (s.f. = 0.68)	Dim. Para. (s.f. = 0.76)	Regress. Eqn. (s.f. = 0.62)	Dim. Para. (s.f. = 0.62)	Regress. Eqn. (s.f. = 0.63)	Dim. Para. (s.f. = 0.71)	Regress. Eqn. (s.f. = 0.62)
Average	28	28	263	214	74	75	586	512
Minimum	14	14	162	132	13	13	182	159
Maximum	54	54	429	350	226	230	1393	1216

[a]Italic text for identifiers 35E.a, b, and c signify that those three SRs reaches are part of a single network (Area_35E). Bold text designates those SRs with wavelength-to-width ratios more than ~25% below or above the range of average terrestrial values (discussed in section 3.3.2). 'Dim. Para.' refers to gravitational scaling factors derived from dimensionless parameters, 'Regress. Eqn.' refers to gravitational scaling factors derived from manipulation of regression equations (discussed in Appendix B), and 's.f.' refers to the scaling factor values used. The values in parentheses show the total error in m^3 s^{-1} scaled for Martian gravity.

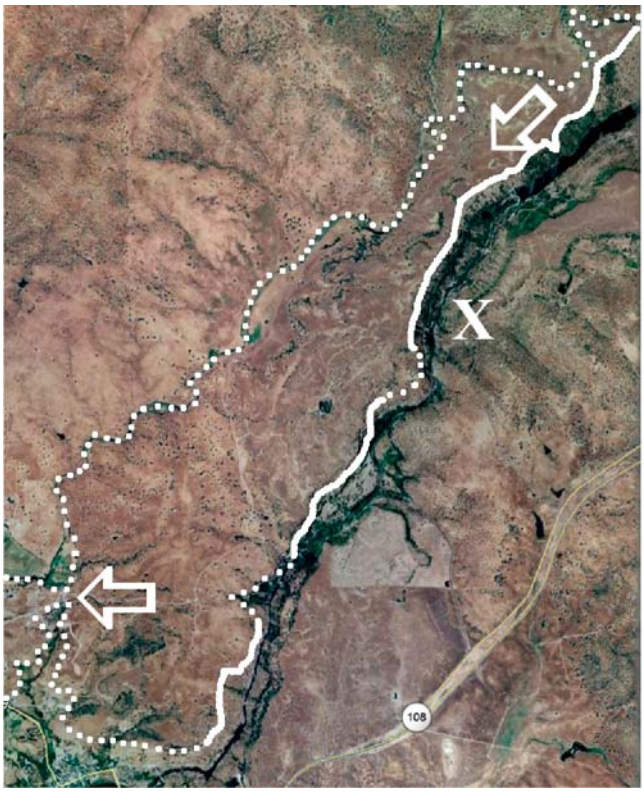

Figure 6a. Plan view of the terminus of the Stanislaus Table Mountain (STM), near 370 30′ N 1200 50′ W, southeast of Jamestown, California, USA. The direction of inflow was from the upper right corner; outflow occurred at the lower left edge (white arrows). The white line (dashed where approximate) outlines the inferred area of ponding. The white 'X' denotes the location from which the images comprising Figure 6b were taken looking southwest. The four-lane highway in the lower right, labeled '108' provides an indication of scale. Google Earth imagery ©Google Inc. Used with permission.

averaged values are given in Table 1 and shown graphically in Figure 5. Three of these SRs were for conjoined reaches within of a single branching network of multilevel SRs (Area35_E), distinguished in Table 1 with italic font. The remaining SRs in Table 1, three of which formed the superjacent thin SR of a multilevel SR, were all single reaches.

3.3.6. Error Analysis

[36] Two different sources of error introduce uncertainty into these discharge estimates. The regression equations have standard error given in percent (see Appendix A). In addition, error is associated with the collection of the data. These errors may be combined by addition in quadrature [*Taylor*, 1982]. Discussion of this approach is provided in Appendix C. The results of our error analysis are shown in parentheses in Table 1.

4. Results

[37] First, we present our results from the thermal inertia derivation, which support the interpretation of fluvial SR formation through inversion. Next, we use a morphologic analysis, based on terrestrial analogs, to infer the likely inversion mechanism. Then we present the results of our paleodischarge estimates for thin SRs.

4.1. Thermal Inertia

[38] The overall accuracy of THEMIS thermal inertia is expected to be 15–20% due to uncertainties in albedo, slopes, atmospheric pressure, and other factors (see *Fergason et al.* [2006] for a full description). This 15–20% uncertainty was considered the minimum difference between a given SR and the surrounding terrain necessary to positively identify an indurated SR. Most SRs are near the limit of detection at THEMIS spatial scales. The majority of those detected have consistent thermal inertia values of 250–350 J m^{-2} K^{-1} $s^{-1/2}$ or SI thermal inertia units (hereafter referred to as tiu), with the surrounding terrain having thermal inertia values several tens (~40–60) of tiu lower. A small number of SRs are more thermally distinct, showing differentials of up to a few hundred tiu from the surrounding terrain (e.g., Figures 3a–3c).

[39] The MFF is located within the generally dusty equatorial regions, with moderate to high dust cover as indicated by dust cover index derived from Thermal Emission Spectrometer (TES) data [*Ruff and Christensen*, 2002]. Therefore, the derived thermal inertia values are likely that of a mixed surface (dust and bedrock), although because of the difference in resolution between THEMIS (100 m px^{-1}) and TES (3 km px^{-1}) dust-free bedrock exposures on the scale of THEMIS pixels are possible. Consequently, we interpret the derived thermal inertia to be minimum values for the material underlying the dust cover.

[40] Flat and multilevel SRs are generally a few hundred meters or more in width, so all flat and multilevel SRs were expected to be apparent in night IR images as elevated brightness temperatures, although this expectation was not universally born out. Roughly one-half of ~70 flat and multilevel SRs were identified as having values discernibly higher than the surrounding terrain (Figure 3a). For these SRs, the elevated thermal inertia values imply an increased thermal conductivity, specific heat, and/or density over that of the surrounding materials. This increase in thermophysical properties could be an effect of any of the three possible induration mechanisms, namely, lava in comparison with sediments, cemented sediments in comparison with uncemented sediments, and larger grain sizes in comparison with smaller grain sizes. Thus, elevated thermal inertia values support the inference based on morphology that the fluvial SRs are more resistant to erosion than the surroundings. The remaining half of all flat and multilevel SRs failed to show discernable difference in thermal inertia values. In this dusty region, this lack of signal is attributable to a locally thicker dust cover, although the spatial resolution of the TES-derived dust cover index map [*Ruff and Christensen*, 2002] in comparison to the size of the SRs prevents easy investigation of this idea.

[41] Although most flat and multilevel SRs stand a few tens of meters above the surrounding terrain (e.g., Figure 2c), a few broad and flat-topped SRs do not stand significantly higher than the surroundings and were first identified morphologically only through a sinuous pattern on the surface (Figure 3b). These uninverted or only slightly inverted features also show elevated thermal inertia values relative to

Figure 6b. Mosaic of ground photos showing the profile of the area of terminal widening outlined in Figure 6a. The white line (dashed where inferred) denotes the approximate contact between the overlying Table Mountain lava and the underlying fluvial sediments. Both the lava and the sediments are cliff-formers in this location. White box in lower right shows vehicle (on the shoulder of Tulloch Dam Road), which gives an indication of scale.

their surroundings (Figure 3b). Although confined to only a few examples to date (other candidates include Area23_A and Area39_A) [see *Burr et al.*, 2009, Table 1], this finding provides significant evidence to substantiate the hypothesis that the SRs are more indurated and therefore resistant to erosion than the surrounding material.

[42] The widths of thin SRs are usually near or below the limit of THEMIS IR resolution and so are usually not discernable in thermal inertia images (e.g., Figure 3a, upper left). However, almost 20% of thin SRs had higher thermal inertia values than the surrounding terrain (Figure 3c). Even some thin SRs that transition into disconnected knobs due to aeolian abrasion also showed higher thermal inertia than the surrounding terrain (Figure 3c). On their long sides, these knobs are the equivalent of 2–3 pixels (roughly 200–300 m) in THEMIS IR images, which is at the discernment limit for thermal inertia images. Thermal inertia may be elevated in these cases because of increased induration that creates these knobs and/or a longitudinal orientation of the knobs, which would enhance thermal response. Comparison of visible and nighttime IR images shows that the more extensive coverage of IR images, even at lower resolution and longer wavelengths, may reveal additional SRs.

4.2. Inversion Mechanism

[43] Inversion occurs through localized induration of the channel bed followed by regional erosion of the surrounding terrain.

4.2.1. Induration Mechanism

[44] Each of the three possible induration mechanisms – chemical cementation, armoring, and lava infill – exhibit specific morphologies in terrestrial examples. Intercomparison of these terrestrial morphologies with typical fluvial SR morphologies in the AZP can be used to indicate the most likely induration mechanism.

4.2.1.1. Lava Infill

[45] The AZP region is bounded on the north by the lava-filled Cerberus plains (Figure 1), and so contextually lava capping may be a viable induration mechanism at least for those SRs found at lower elevations. Lava-capped valleys of Pleistocene age are found near St. George, Utah, United States [*Williams and Irwin*, 2009], and lava-infill of a late Tertiary paleochannel produced the Stanislaus Table Mountain (STM) in northern California, United States [*Rhodes*, 1980, 1987; *Burr and Williams*, 2009]. These two terrestrial examples suggest some criteria for identifying fluvial feature inversion by lava infill.

[46] Morphologically, these lava-capped features show significant variation in width (up to an order of magnitude). The lava-capped ridges near St. George show localized variation in width over short distances and an overall increase in feature width over baselines of several kilometers, changes hypothesized to have resulted from variation in the paleovalley shape and lava ponding behind obstacles [*Williams and Irwin*, 2009]. Mapping of the STM [*King et al.*, 2007, Figure 1] shows an overall increase in width with distance downslope. Field reconnaissance shows that near the terminus of the mapped flows, an area of increased width, which has been exposed by modern fluvial erosion, corresponds to an increase in lava flow depth (Figures 6a and 6b). From the combination of plan and profile views, this area of flow expansion is interpreted as a region where the lava overflowed the channel and ponded within the surrounding alluvial valley. Another common morphological indication of lava capping may be columnar jointing, which is visible both in the St George lava cap and in the STM latite lava, where it facilitates fracturing along planes of weakness. Failure along these planes of weakness produces basal rubble piles of jointed lava up to several tens of meters in width along the sides of the Table Mountain (Figures 7a and 7b). Contextually, the lavas that fill these paleochannels have been traced to local sources. The STM latite is attributed to the Little Walker caldera [*King et al.*, 2007], and the lava capping the St George paleochannels has been traced to cinder cones in the Pine Mountain Valleys [*Biek et al.*, 2007]. Last, a lava cap

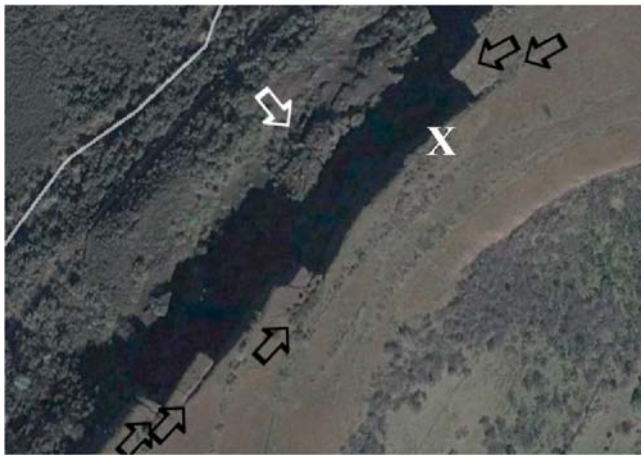

Figure 7a. Plan view of STM near 37° 55′ 40″ N 120° 27′ 40″ W showing collapse of lava along fissures (black arrows) within the columnarly jointed lava. Illumination is from the lower right, so much of the basal rubble pile along the northern side is in shadow. However, a few large slabs of lava are visible to the upper right of the shadow (white arrow). White 'X' denotes location atop the STM from which the image in Figure 7b was taken looking west–southwest. Grey line at upper left denotes a two lane dirt road (Peoria Flat Road), which gives an indication of scale. Google Earth imagery ©Google Inc. Used with permission.

would be expected to obscure any surface fluvial textures, e.g., scroll bars.

[47] Few of these morphologic or contextual indications of lava-capping are apparent for the inferred fluvial SRs in the AZP. No obvious volcanic source that could provide lava capping is visible in available images, although extensive burial and erosion may have obscured any such sources. Several flat and multilevel SRs show fluvial textures in the form of semi-concentric lineations, inferred to be scroll bars [*Burr et al.*, 2009], indicating that a surface fluvial texture has not be obscured by capping lava. Columnar jointing is discernable in other regions on Mars at the resolution of HiRISE images [*Milazzo et al.*, 2009], but is not observed in the AZP SRs in available high-resolution images. A limited number of SRs do show significant terminal widening (e.g., Figure 3a) as observed for the STM, and those SRs may be candidates for lava-capped inverted fluvial feature. This bulbous morphology is limited to only ~5% of the inferred fluvial SRs.

[48] In addition, the observed thermophysical properties do not appear consistent with lava capping. The SR apparent thermal inertia values, with the range of ~100–300 tiu, are about an order of magnitude lower than what would be expected for a pristine basalt lava flows (2215) [*Fergason et al.*, 2006, Table 5]. Dust cover may mask the true thermophysical properties of the underlying SR material, reducing the thermal inertia [*Fergason et al.*, 2006]. However, these observed low thermal inertia values occur even for SRs with low dust coverage [*Ruff and Christensen*, 2002], in southern portion of AZP (e.g., Area 23_A, shown in Figure 3b).

[49] Thus, on the basis of dissimilar surface texture, dissimilar SR morphology, apparent lack of a lava source, and observed thermophysical properties, lava capping appears an unlikely induration mechanism in general for these Martian fluvial features. The northern-most SRs, located on the volcanic Cerberus plains, may be a lava channel (Area 26) [*Burr et al.*, 2009], and the ~5% of the fluvial SRs that have bulbous terminations may have been indurated by lava capping. Continued examination with new images of the AZP region may provide evidence of possible lava sources. For the majority of inferred fluvial SRs (e.g., Figure 2), however, morphological evidence to support the hypothesis of lava-infilling is lacking.

4.2.1.2. Armoring

[50] Another possible induration agent for the fluvial SRs is coarse-grained lag deposition or clast armoring. On Earth, inversion of paleochannels or valleys by armoring appears less common than by cementation or lava capping, and only a limited number of examples have been documented in low-relief settings. Flooding events in a river system can produce imbricated clasts and pebble clusters. These deposits are often preserved in the sedimentary record and serve to armor the river-bed [*Reid et al.*, 1997; *Jones and Frostick*, 2008], although they typically have a non-uniform distribution along the river-bed. From the limited terrestrial examples of inversion due to clast armoring, however, some fundamental observations may be made with respect to the AZP SRs.

[51] Armoring has been documented in the eastern United States. Armored ridges or 'noses' found in southwestern Virginia, United States, are interpreted as paleovalleys or 'dells' where boulder deposits have caused topographic inversion [*Mills*, 1981, 1990]. These inverted landforms are located on mountain slopes of a few tens of degrees and extend several hundred meters in length [*Mills*, 1981]. Another example of inversion due to armoring was documented on road cuts near Tucson, Arizona, USA [*Osterkamp and Toy*, 1994]. The road cut design slopes were initially 40–50 degrees, providing the shear stress necessary for coarse

Figure 7b. Ground photo of the rounded slabs of lava and surrounding basal rubble shown in Figure 7a. Tree branch in the middle is ~0.3 m in diameter for scale.

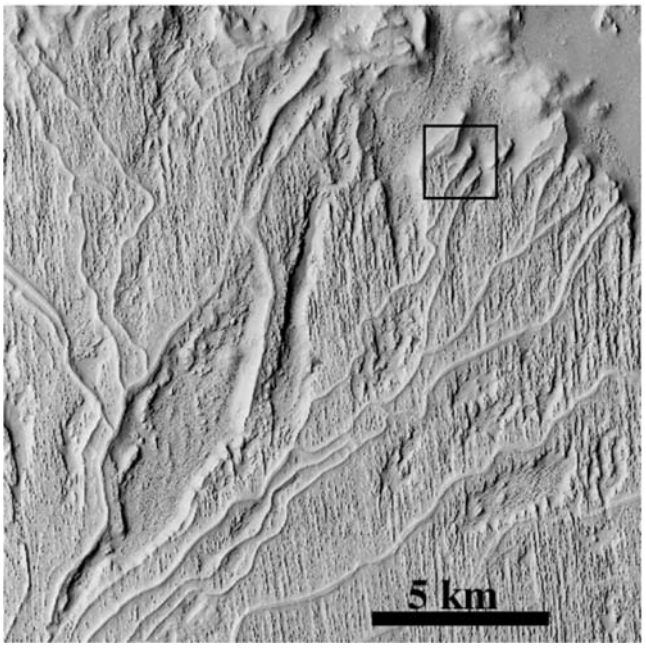

Figure 8a. Portion of CTX image P03_002279_1737_XI_06S208W, showing part of Area43_C, a branching network of thin SRs (see *Burr et al.* [2009, Figure 6b] for an overall view of the network). The box shows the location of Figure 8b. The wide-spread north–south striping is a result of aeolian abrasion. Illumination is from the west (left).

grain transport, although slope reduction during the ongoing inversion process lowered these angles by roughly 10–20 degrees. The length of the armored section was on the order of several meters [*Osterkamp and Toy*, 1994].

[52] In comparison to these terrestrial landforms created by clast armoring, the MFF slopes that host SRs are considerably less steep, with maximum values of less than a few degrees as shown by gridded MOLA topography. The lengths of the SRs are also considerably longer, extending up to tens of kilometers. Morphologically, the terrestrial inverted paleovalleys have a broadly sloping or rounded morphology, whereas the fluvial SRs commonly have sharp rims and steep sides. In Utah, cemented paleochannels transition from a flat topped to a rounded morphology, but these stretches generally occur where the capping cemented layer has been removed, allowing the underlying sediments to be eroded [*Williams et al.*, 2009; see also *Burr et al.*, 2009, Figure 10]. In Oman, coarse gravel deposits create steep-sided Plio-Pleistocene-age paleochannels, but those deposits are heavily cemented by calcite precipitated from groundwater [*Maizels*, 1987]. Thus, documented terrestrial examples of armoring without the cohesion provided by cementation do not show the steep-sided morphology and linear extents observed for the fluvial SRs on shallow slopes in the AZP. The AZP region does host a small number of rounded SRs, for which hypotheses are discussed by *Burr et al.* [2009]. However, for the inferred fluvial SRs, morphological evidence consistent with primary formation by coarse-grained sediment armoring is lacking.

4.2.1.3. Chemical Cementation

[53] In comparison with lava-capping and armoring, chemical cementation would be best expected to preserve fluvial sedimentary structures. For example, inverted cemented paleochannels in Oman and in east-central Utah have preserved their paleopoint bar deposits [*Maizels*, 1987; *Williams et al.*, 2007]. The available HiRISE data of thin SRs provide morphological evidence for cementation of sedimentary layers, including a flat-topped morphology (Figures 8a and 8b). The sides of the SRs are generally sloping, but fine-scale layering is also visible (Figure 8c). Terrestrial cemented paleochannels also show a flat-topped morphology with sloping sides, caused by the presence of an indurated upper layer over less indurated sediments [*Williams et al.*, 2007, 2009]. Although fine layers are rarely exposed in terrestrial examples, the fine layers observed in the AZP SRs are consistent with episodes of sedimentary deposition involving liquid water. Conversely, these observations of the SRs are inconsistent with the lava-capped terrestrial paleochannels, which exhibit steep sides without fine-scale layering and basal rubble piles of columnarly jointed basalt. Thus, surface texture and morphology as observed in available data support the hypothesis that fluvial SR induration is a result of sedimentary cementation. Chemical cementation is generically regarded as the most likely mechanism for terrain inversion on Mars [*Pain et al.*, 2007].

[54] Cementation can result from various processes, including degassing, fluid mixing, cooling, evaporation, and sublimation (see discussion by *Pain et al.* [2007] and references therein). The first three mechanisms would imply a groundwater source for the paleoflow. Degassing produces carbonate cements when groundwater with high partial CO_2

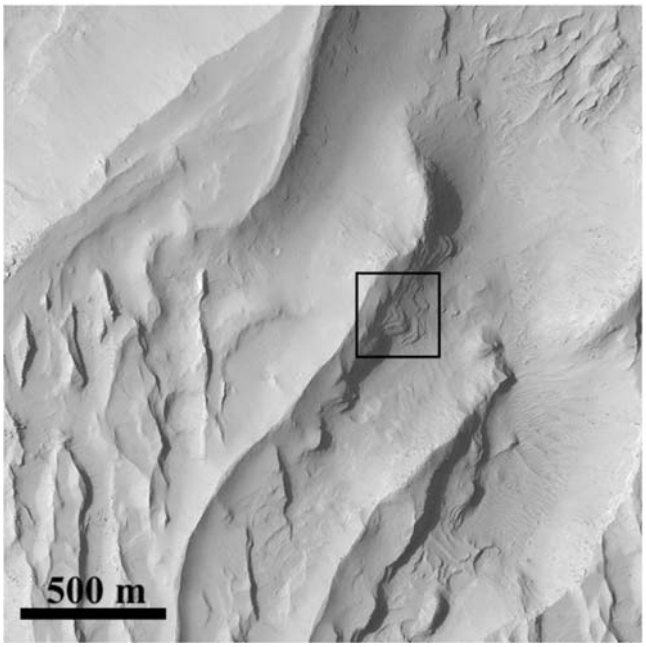

Figure 8b. Portion of HiRISE image PSP_002279_1735, showing layering within a tin SR. Black box shows the locations of Figure 8c.

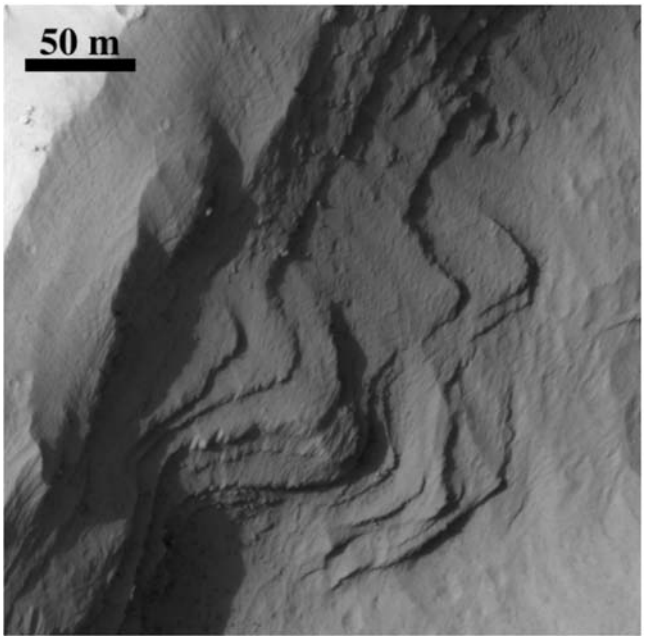

Figure 8c. Portion of HiRISE image PSP_002279_1735, showing thin layering within the SR. The flat-looking layers below the SR are distinct in appearance from the cliffs and rubble piles of columnarly jointed basalt observed around lava-capped channels on Earth.

pressure discharges into the atmosphere. Fluid mixing causes cementation through chemical interaction of groundwater between multiple aquifers. Cooling of deep groundwater as it ascends to shallower levels may also cause chemical precipitation. As the water source for the fluvial AZP SRs is inferred to be rainfall-runoff [*Burr et al.*, 2009], none of these three processes is likely to be the primary cementation mechanism. Cementation through evaporation occurs when fluids are exposed to an undersaturated atmosphere, such that evaporative loss of water causes chemical precipitation. Evaporative loss of near-surface water from saturated fluvial sediments would have been possible during the transition from a humid climate as implied by the SRs themselves to an arid climate such as prevails today. Slow seepage through the shallow subsurface or migration of moisture films may also cause chemical cementation through evaporation. Permittivity values from SHARAD suggest that the upper few hundred meters of the MFF have a high porosity [*Carter et al.*, 2009]. In the presence of flowing surface water, this high porosity material would likely allow either infiltration and subsequent evaporation, or seepage through the shallow subsurface. Thus, chemical precipitation due either to flow in the shallow subsurface and/or evaporative water loss is considered the most likely mechanism for AZP SR cementation. The dry areas between the rivers would not have experienced any infiltration or subsequent evaporation, so would not have been chemically cemented. The final cementation mechanism, sublimation, operates in a similar fashion to evaporation, but requires the transition of pore ice directly into vapor. The fluvial AZP SRs were formed by flowing water, not flowing ice (i.e., glaciers), and there is noticeably little evidence in the region for glacial or periglacial features [*Burr et al.*, 2009]. Thus, this mechanism is not considered likely, although it is difficult to assess its occurrence during possible climatic cooling at the cessation of fluvial activity.

[55] The cementing agent would be difficult to infer from spectroscopy, given the dust cover over the MFF. Carbonate cements are common on Earth. Carbonate-bearing rocks have only rarely been inferred for Mars where they are dated to the Noachian or early Hesperian era [*Ehlmann et al.*, 2008], although the presence of carbonate minerals in the Martian dust [*Bandfield et al.*, 2003] and the multiple hypotheses for carbonate formation on early Mars [e.g., *Niles et al.*, 2005] may indicate wider-spread carbonate source rocks in the past. Silica, iron, and sulfate are prevalent in volcanic ash, so silcrete, ferricrete, or sulfate-rich cements (such as gypsum or jarosite) could each have reasonably been derived from the putative volcanic ash that comprises the MFF. Other possibilities include cementing salts, such as halite, produced during evaporation. Thus, a variety of viable cementing agents that could have derived from the SR host rock exist. However, the dust covering the MFF currently prevents remote determination of the cementing agent.

4.2.2. Erosion Mechanism

[56] On Earth, the differential erosion of paleochannels and alluvial valleys that results in terrain inversion is produced by fluvial erosion and sediment transport. Where inverted fluvial features become infilled with lava or indurated, continued rainfall-runoff produces erosion on either side of the infilled or indurated paleochannel. These twin lateral channels are the primary cause for the differential erosion that results in paleochannel inversion and can be observed in present-day inverted landscapes on Earth [*Pain and Ollier*, 1995].

[57] The western MFF has been inferred to date from the Hesperian to early Amazonian (see discussion and references from *Burr et al.* [2009], also see *Kerber and Head* [2010]). Thus, based on their location within the western MFF, the fluvial features that became the SRs are inferred to have originally formed during this time. The fluvial phase and the subsequent erosion phase could have occurred close in time. Alternatively, the two phases could have been distinctly separated in time, with the fluvial phase occurring in the late Hesperian and the erosional phase occurring during the early Amazonian or possibly later.

[58] Whether the erosional phase occurred in the Hesperian or Amazonian Periods, the erosional process is unlikely to have been rainfall-runoff as on Earth. The putative rainfall that formed the Noachian-aged valley networks did not extend to the late Hesperian or early Amazonian [*Carr*, 1996], and twin lateral channels are not apparent. A few small, negative relief troughs are visible in the MFF in and around some SRs [see, e.g., *Burr et al.*, 2009, Figure 4]. These troughs may indicate fluvial flow subsequent to SR formation, so some additional erosion might have been caused by fluvial entrainment and transport. However, these possible fluvial channels have been observed only in very limited and scattered locations.

[59] The Amazonian Period is widely characterized by aeolian processes, and by an absence of rainfall or sustained

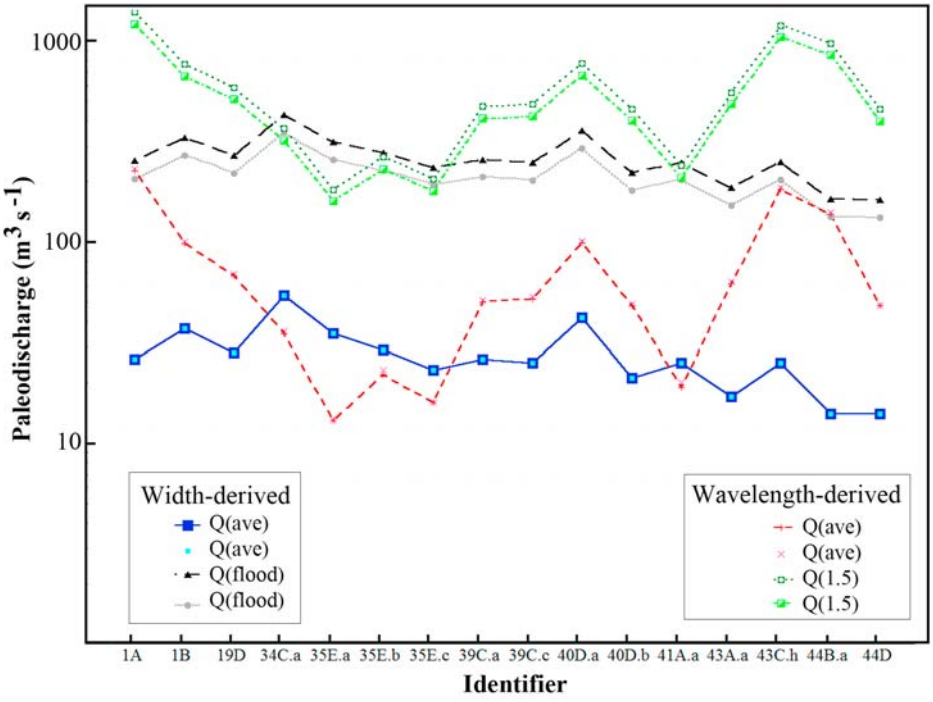

Figure 9. Plot of the paleodischarge estimates shown in Table 1. Two values exist for each of the four paleodischarge types (average or flood, width-derived or wavelength-derived) as a result of two different scaling approaches. In general, the wavelength-derived estimates are higher than the width-derived estimates, suggesting that the width measurements may have been affected by erosion. However, the five identifiers for which the width-derived estimates are higher have wavelength-to-width ratios similar to (uneroded) terrestrial ratios.

fluvial activity. In particular, the meso-scale ellipsoidal landforms that pervade the MFF are interpreted as yardangs, which form through aeolian abrasion [*Ward*, 1979; *Wells and Zimbelman*, 1997; *Mandt et al.*, 2008]. High-resolution images show SRs transitioning into disjointed knobs (e.g., Figures 2a or 3c), which in consonance with the interpretation of the MFF morphology, were inferred to be a result of aeolian abrasion [*Burr et al.*, 2009]. Given the presence of yardangs throughout the western MFF, including their close proximity to SRs (see, e.g., Figure 8a), we infer aeolian abrasion to be the primary mechanism for the differential erosion necessary to have exposed the SRs.

4.3. Paleodischarge Calculations

[60] For the 16 thin SR reaches for which discharge values were estimated, the average daily discharge with error estimates ranged from 2 $m^3 s^{-1}$ to 244 $m^3 s^{-1}$. The average value is 59 $m^3 s^{-1}$, an update from the value provided by *Wendell et al.* [2008]. The estimated discharges for the channel-forming flood ranged from 83 $m^3 s^{-1}$ to 1467 $m^3 s^{-1}$ including error, with an average value of 431 $m^3 s^{-1}$. Table 1 lists the numerical values and Figure 9 provides a graphic presentation of the individual results.

[61] In the large majority of cases, the average paleodischarge values estimated from the two different measurements – width and wavelength – are within a factor of a few. In 11 of the 16 cases, the paleodischarge value estimated from width measurements was less than the value estimated from wavelength measurements, and the average value estimated from width is only one-third of the average value estimated from wavelength. This discrepancy might reasonably be caused in part by an unknown amount of erosion of SR width, with the wavelength estimates providing the more accurate result. We note, however, that all five of these cases in which width-derived values exceed wavelength-derived values are considered higher precision reaches (i.e., having wavelength-to-width ratios within ~50% of the terrestrial average).

[62] A noticeable difference exists between average paleodischarge estimates for SRs having a wavelength-to-width ratio within ±25% of the average terrestrial range of values (denoted without bolding in Table 1; see Figures 4 and 5) and those outside this envelope (denoted by bolding in Table 1). Among the former, the percentage difference in discharge estimates calculated from width and from wavelength ranges ±6% to 23%. Among the latter, the percentage difference in discharge estimates calculated from width and from wavelength ranges from ±19% to 41%. In other words, the discharge estimates derived from SRs with wavelength-to-width ratios similar to terrestrial ratios cluster more tightly than the discharge estimates derived from SRs with larger wavelength-to-width ratios. Inasmuch as the increased clustering implies increased precision, this result suggests the utility of using the wavelength-to-width ratio as a criterion for evaluating erosion.

[63] Because of their different recurrence intervals (2-year versus 1.5-year), direct comparison between the channel-forming flood values derived from the SR width (equation (A2)) and the channel-forming flood values derived from SR wavelengths (equation (A4)) cannot be made. However, the former should all be larger than the latter, because 2-year floods should be larger than 1.5 year floods. However, this relationship is true in only one-quarter of the cases (Table 1). An unknown amount of erosion associated with width could account for the smaller channel-forming flood values derived from width, despite our efforts to screen out highly eroded SRs through use of a wavelength-to-width ratio criterion. The terrestrial recurrence intervals for these two channel-forming floods do not imply any particular recurrence interval for channel-forming floods on Mars.

5. Summary and Implications

[64] In this work, we present an analysis of the formation mechanism for the inferred fluvial SRs in the AZP region, located largely within the western MFF. Morphological comparison with terrestrial analogs and thermal inertia data of the fluvial Martian SRs support a previous hypothesis of inversion, involving induration of fluvial channels and meander belts followed by subsequent erosion of the less resistant surrounding terrain as the primary formation mechanism for the thin, flat, and multilevel SRs. Surface sedimentary structures and fine-scale layering suggest that for the large majority of examples, induration occurred through cementation of fluvial sediments. In contrast, columnarly jointed basalts, basal rubble piles and other evidence for lava infill are not discerned, although a few SRs with bulbous terminations may be candidates for lava capping. Nor are morphological attributes consistent with terrestrial examples of induration through clast armoring. Thermal inertia values for about one-half of all flat and multilevel SRs are elevated by a few tens of tiu up to a few hundred of tiu over values for the surrounding terrain, consistent with the hypothesis that the SRs are composed of more indurated material than the surrounding terrain. However, not all flat and multilevel SRs have noticeably higher thermal inertia values, attributable either to a heterogenous dust cover or to variation in the thermophysical properties of the SRs. Some thin SRs, eroded into an alignment of disjointed knobs, are near the spatial resolution of the IR images, yet are nonetheless distinct in thermal inertia data. Enhanced cementation and/or orientation may be the causes for these elevated temperatures.

[65] The exact nature of the chemical cements is currently unknown. The most likely candidates – silcrete, ferricrete, or evaporatic duricrusts – all involve the presence of water, although the role of water differs in each case. This chemical cementation is hypothesized to have resulted either from slow groundwater seepage through and/or evaporation from the fluvial sediments. Following induration by chemical cementation, these paleochannels and floodplains were likely exposed primarily by aeolian abrasion of the less indurated surrounding MFF, although some erosion may have been effected by limited fluvial processes. Thus, the Aeolis/Zephyria Plana fluvial SRs were most likely produced through induration by chemical cementation and subsequent erosion by wind, in agreement with the conclusion of *Pain et al.* [2007].

[66] Measurements of width and wavelength for well-preserved thin SRs yield paleodischarge estimates through use of empirical relationships for terrestrial rivers scaled for Martian gravity. In view of the extensive erosion of the MFF, the ratio of wavelength-to-width was used to exclude excessively eroded SRs from paleodischarge estimates. In about one-half of the cases, the channel-forming 2-yr-flood values estimated from empirical relationships based on width, are less than the channel-forming 1.5-yr-flood values estimated from empirical relationships based on wavelength. In a flood series record for any given river, the 2-year flood value should necessarily always exceed the 1.5-year flood value. Thus, this comparative result suggests that erosion may indeed have affected (reduced) SR widths, so that our paleodischarge estimates based on widths may be minima. This comparative result also points to the importance of applying some criterion, such as terrestrial-like values for wavelength-to-width ratios used here, for assessing erosion. However, for any given SR, a lower number of wavelength measurements are generally possible, especially in heavily eroded landscapes like the MFF, because of limited feature preservation. This lower number of measurements yields greater errors for paleodischarge estimates based on wavelength measurements than for those based on width measurements. This fact provides another consideration during collection of data from inverted or exhumed paleochannels for paleodischarge estimation.

[67] For those SRs meeting a set of criteria for paleodischarge estimates, our initial formative flood paleodischarge values generally range between 10^1 to 10^3 m^3 s^{-1}. The higher of these values are comparable to paleodischarge estimates for floods that formed late-stage Noachian fluvial deposits and valley networks on Mars [*Moore et al.*, 2003; *Irwin et al.*, 2005]. As the MFF is age-dated as late Hesperian to early Amazonian, this comparison indicates that at least within this region, fluvial processes sometime during this age-range were similar in magnitude to fluvial processes in the late Noachian.

[68] The erosive environment in which these SRs exist today largely precludes information on drainage areas; likewise, for the SRs for which we estimate paleodischarge, significant areal sediment deposits are not apparent. Thus, information is lacking with which to estimates flow duration for these fluvial SRs. However, the high sinuosity of some these SRs (three examples have sinuosities of ~2 or above) suggests flow at least on the time scale of a few years. Data indicate that terrestrial point bars require $\geq 10^2$ years to form [e.g., *Hickin*, 1974; *Rodnight et al.*, 2005; *Tooth et al.*, 2009], although in rivers with steeper gradients point bars may form within a few years. MOLA data over a limited number of SRs [e.g., *Burr et al.*, 2009, Figure 7] indicate that SR gradients today are generally low (0.001 to 0.005). Given a similar rate of sediment entrainment and transport on Mars as on Earth [*Komar*, 1980; *Burr et al.*, 2006a], the inferred relict point bars preserved on the surface of flat SRs connote a similar duration of flow. The complex stratigraphic relationships and wide elevational range (over 3500 m) [*Burr et al.*, 2009] of the fluvial SRs suggest that this aqueous formation process operated over an extended period of time. They also imply continual fluvial activity

during emplacement in this region of the MFF. This population of SRs extends over an area of close to 200,000 km^2, although SR density varies considerably within this area [*Burr et al.*, 2009]. Thus, these SRs provide evidence for precipitation runoff and fluvial activity continually, though possibly episodically, over 10^1 to 10^3 years and over a significant geographic area. This result provides important information on the atmospheric and climatic conditions at this equatorial location around the Hesperian-Amazonian transition.

[69] Future work will expand these initial estimates. Paleodischarges will be estimated for other fluvial SRs, namely, flat SR, interpreted as inverted floodplains. The approach used in this initial work is applicable only to discrete river channels, hence, the focus of this work only on well-preserved thin SRs. For meander belts, paleodischarge estimates may be derived [*Williams*, 1988] through the use of high-resolution data to accurately determine meander dimensions [e.g., *Brookes*, 2003]. Future work will utilize high-resolution images in order to derive paleodischarges for flat SRs. In cases of multilevel SRs, thin SRs superposed upon flat SRs, the comparison of paleodischarge values for the sub- and the superjacent SRs will provide an indication of change in flow conditions with time, with implications for climatic processes in the Hesperian to Amazonian epochs.

Appendix A: Terrestrial Form-Discharge Relationships

A1. Average Daily Discharge and Channel-Forming Flood Discharge Estimates Based on Width

[70] For 252 sites on rivers in the Missouri River basin in the west-central United States, *Osterkamp and Hedman* [1982] derived discharge relationships as a function of channel dimensions. The relationship between channel width and discharge was determined to be

$$\overline{Q} = 0.027 W_b^{1.71}, \tag{A1}$$

where $\overline{Q}$ is the average daily discharge in m^3 s^{-1} and W_b is the (bankfull or active) channel width in meters [*Osterkamp and Hedman*, 1982, Table 3]. This equation was derived at sites with widths between 0.8 m and 430 m, so that this range of widths is a criterion for valid use of this equation. The standard error for this equation is 79%. This equation provides the simplest relationship between average daily discharge and width, having been derived for bed and bank material of various sizes.

[71] In the same study, the relationship between channel width and the channel-forming flood discharge (in this case, of the 2-year flood) was derived as

$$Q_2 = 1.9 W_b^{1.22}, \tag{A2}$$

where Q_2 is the biannual flood discharge in m^3 s^{-1} [*Osterkamp and Hedman*, 1982, Table 3]. Derived from the same 252 sites, this relationship likewise applies to channel widths in the same range and to a variety of bed and bank material sizes [*Osterkamp and Hedman*, 1982]. The standard error for this equation is 109%.

[72] For both the average discharge and the channel-forming flood discharge, more precise correlations were derived based on bed and bank sediment size, although the standard error was not noticeably decreased for all sediment sizes [*Osterkamp and Hedman*, 1982]. Given the current uncertainties in MFF grain size, application of these more precise relationships is not warranted here.

A2. Average Daily Discharge and Formative Flood Estimates Based on Meander Wavelength

[73] In addition to width, meander wavelength can also be used to estimate both an average discharge and a formative flood discharge (summarized by *Williams* [1988]). Using wavelengths to estimate discharge provides a check on the discharge estimates derived from channel widths. *Carlston* [1965] examined the relationship between meander wavelength and discharge for 31 rivers located mostly in the central United States. The relationship between the meander wavelength and the average discharge was calculated as

$$\overline{Q} = 0.000017 L_m^{2.15}, \tag{A3}$$

where L_m is the meander wavelength in meters (*Carlston* [1965], modified by *Williams* [1984]). The applicable range of L_m values for which this equation was derived and to which it may be applied is 145 m to 15.5 km. The standard error is 26%.

[74] For estimation of a channel-forming flood discharge, the correlation with meander wavelength for 28 river reaches in the central U.S. is given as (*Carlston* [1965], modified by *Williams* [1984])

$$Q_{1.5} = 0.011 L_m^{1.54}. \tag{A4}$$

In this instance, the channel-forming flood discharge was taken by Carlston as the 1.5-year flood, or the maximum flood with an average recurrence interval of eighteen months. As with the previous equation from *Carlston* [1965], the applicable range of L_m values for this correlation is 145 m to 15.5 km. The standard error is 41%.

Appendix B: Scaling for Martian Gravity

[75] We present two different techniques to scale these terrestrial empirical equations for Martian gravity. The close similarity of the results from the two methods suggests the correctness of those results.

B1. Dimensionless Flow Parameters

[76] Flow parameters may be rendered in dimensionless form through a dimensional (or units) analysis approach. For example, flow width may be rendered dimensionless through multiplication by gravity to the one-fifth power and division of discharge to the two-fifths power [*Parker et al.*, 2007]. An analysis of data from gravel bed terrestrial rivers involving dimensionless flow parameters suggests that width scales with gravity to the −0.233 power [*Parker et al.*, 2007, equation (13)], so that

$$\frac{W_{ET}}{W_E} \propto \left(\frac{g_{ET}}{g_E}\right)^{-0.233}, \tag{B1}$$

where subscripts *ET* and *E* denote extraterrestrial and Earth, respectively. Moving from terrestrial to Martian gravita-

tional acceleration, the amount by which W (or L_m) should be increased for a given discharge is $(g_{Mars}/g_{Earth})^{-0.233} = (3.7/9.8)^{-0.233} = 1.25$. This increase in width by 1.25 times the original width may then be inserted into the empirical equations to derive the scaling factors for the discharge [cf. *Moore et al.*, 2003].

[77] For example, inserting a factor of 1.25 for the width into equation (A1) gives

$$Q = 0.027(1.25W)^{1.71} = 0.027(1.25)^{1.71}W^{1.71} \quad \text{(B2)}$$

$$Q(1.25)^{-1.71} = 0.027W^{1.71}. \quad \text{(B3)}$$

On the basis of this reasoning, Q values in Table 1 derived using equation (A1) are scaled using this first approach by $(1.25)^{-1.71}$ or 0.68. By analogous reasoning, the scaling factor for equation (A2) is $(1.25)^{-1.22}$ or 0.76. The scaling factor for equation (A3) is $(1.25)^{-2.15}$ or 0.62. The scaling factor for equation (A4) is $(1.25)^{-1.54}$ or 0.71. These scaling factors are listed in Table 1.

[78] The basis for this scaling is a data set collected from gravel bed rivers [*Parker et al.*, 2007]. As the grain size of the material in the MFF is hypothesized to be finer-grained volcaniclastic sediments, this use of data from river beds with larger grains may introduce some error into these estimates. However, this approach is used as an additional method for deriving scaling values and the close agreement between these scaling factors and those derived immediately below suggests the viability of the results.

B2. Manipulation of Regression Equations

[79] An alternative approach to scaling for Martian gravity involves manipulation of regression equations [cf. *Irwin et al.*, 2008]. Regression equation manipulation is demonstrably erroneous when the equations are inverted to solve for the independent variable [*Williams*, 1983]. However, rearrangement and recombination of the parameters can provide some indication of their relative importance. Setting each empirically derived terrestrial expression for discharge equal to the Darcy-Weisbach equation allows for determination of the factor by which width must increase under reduced gravity. As with the first approach, this factor can then be substituted back into the empirical expression to yield the overall scaling factor for discharge.

[80] For example, setting equation (A1) equal to the Darcy-Weisbach equation (equation (1)) gives

$$H^{1.5}W\left(\sqrt{8gS/f}\right)^{0.5} = 0.027W^{1.71}. \quad \text{(B4)}$$

For a given channel, i.e., S, g, and f are constant, the relationship between H and W is

$$H^{1.5} = kW^{0.71}, \quad \text{(B5)}$$

where the generic coefficient k incorporates all the constants in the equation. Therefore,

$$H \propto W^{0.47} \quad \text{(B6)}$$

so that from substitution of this proportionality back into the Darcy-Weisbach equation

$$Q = \left(kW^{0.47}\right)^{1.5}W\left(\sqrt{8gS/f}\right)^{0.5} = kW^{1.71}g^{0.5}. \quad \text{(B7)}$$

Thus, a reduction in g from terrestrial to Martian values would decrease Q by $(3.7/9.8)^{0.5}$ or 61% of its terrestrial value. To fully compensate, the expression of W in equation (A1) would need to increase to 161% of its terrestrial value

$$W^{1.71} = 1.61 \quad \text{(B8)}$$

$$W = 1.61^{1/1.71} = 1.25. \quad \text{(B9)}$$

Therefore, when using equation (A1), W on Mars must increase by 1.25 times its terrestrial value for a given Q. Conversely, Q must decrease by the same factor for a given expression of W. That this factor of 1.25 is the same value as derived from the first approach appears to be coincidence, and applies only to equation (A1). This factor leads to the same calculations shown in equations (B3) and (B4), so that Q values in Table 1 derived using equation (A1) are scaled by $1.25^{-1.71}$ or 0.68. By analogous reasoning, the scaling factor for equation (A2) is derived from $(1.61)^{1/1.22} = 1.48$, and $(1.48)^{-1.22} = 0.62$. The scaling factor for equation (A3) is derived from $(1.61)^{1/2.15} = 1.24$, and $(1.24)^{-2.15} = 0.63$. The scaling factor for equation (A4) is derived from $(1.61)^{1/1.54} = 1.36$, and $(1.36)^{-1.54} = 0.62$. These scaling factors are listed in Table 1.

Appendix C: Error Analysis

[81] Two different sources of error introduce uncertainty into these discharge estimates. The regression equations have standard error given in percent (see Appendix A). This percent standard error characterizes the unexplained deviation of the actual value of the dependent variable from its expected value based on the regression function. In other words, the standard error quantifies the scatter of the data around the empirical fit. The percent standard error was multiplied by each paleodischarge estimate in order to characterize the error in each estimate.

[82] Error is also associated with the collection of the width and wavelength data. We attempted to minimize these errors and improve accuracy by taking multiple measurements where possible and averaging them. In such cases, this measurement error was taken as the standard deviation of the mean (SDOM), or the standard deviation of the measurements divided by the square root of the number of measurements [*Taylor*, 1982]. Width measurements for each SR ranged in number from 6 to 16. Reliable wavelength measurements for each SR were more difficult to find, as they required a longer section of the SR to be well preserved. In some cases, only one wavelength measurement per SR was possible. Data were taken only on images in which the SRs could be seen clearly (i.e., the SRs were not obscured by atmospheric dust, poor contrast, or other causes outside of geologic considerations), and only well-preserved SRs were measured as discussed above. Thus, for those SRs with only a single measurement, we consider the measurement error to be within one pixel at either end of the mea-

surement, or 36 m. However, we note that a measurement error of 36 m is in all cases lower than the SDOM for wavelength (Table 1), suggesting that using this approach may underestimate the actual error. To estimate paleodischarge error, we used standard methods for propagation of uncertainty, taking the derivative of the discharge equations with respect to width/wavelength and multiplying by the measurement error [*Taylor*, 1982, p. 62].

[83] The total error from multiple sources may be calculated using addition in quadrature, or as the square root of the sum of the squares [*Taylor*, 1982]. For equations (A1) and (A2), the percent standard errors are 79% and 109%, respectively. Based on the number of width measurements (between 6 and 16) per SR, the paleodischarge error is in all cases less than a few percent. Thus, for equations (A1) and (A2), the total error is dominated by the percent standard error of the regression equations. For equations (A3) and (A4), the percent standard errors are 26% and 41%, respectively. For these equations, which are based on wavelength, the paleodischarge error tends to be higher because fewer wavelength than width measurements were possible. Thus, for equations (A3) and (A4), the total error tends to be more evenly divided between the percent standard error of the regression equations and the measurement error. Finally, this total error is multiplied by the appropriate scaling factors to convert to Martian conditions. The results are shown in parentheses in Table 1.

[84] **Acknowledgments.** This work was supported by the Mars Data Analysis Program grant NNX08BA24G. Partial funding for RMEW was provided by Mars Fundamental Research Program grant NNX06AB21G. Funding for KDW was provided by a Research Experience for Undergraduates grant from the NSF to the SETI Institute. We thank Nathaniel Putzig for use of his thermal inertia lookup table and Ross Irwin for helpful discussion. Maarten Kleinhans, Bob Craddock, and two anonymous reviewers provided helpful and constructive comments.

References

Bandfield, J. L., T. D. Glotch, and P. R. Christensen (2003), Spectroscopic identification of carbonate minerals in the Martian dust, *Science*, *301*(5636), 1084–1087, doi:10.1126/science.1088054.

Biek, R. F., et al. (2007), Interim geologic map of the St. George 30′ × 60′ quadrangle and the east part of the Clover Mountains 30′ × 60′ quadrangle, Washington and Iron Counties, Utah, *Utah Dep. Nat. Resour. Open File Rep. 478*, pp. 1–70, Utah Geol. Surv., Salt Lake City.

Bradley, B. A., S. E. H. Sakimoto, H. Frey, and J. R. Zimbelman (2002), Medusae Fossae Formation: New perspectives from Mars Global Surveyor, *J. Geophys. Res.*, *107*(E8), 5058, doi:10.1029/2001JE001537.

Brookes, I. A. (2003), Palaeofluvial estimates from exhumed meander scrolls, Taref Formation (Turonian), Dakhla region, Western Desert, Egypt, *Cretaceous Res.*, *24*(2), 97–104, doi:10.1016/S0195-6671(03)00033-8.

Burr, D. M., and R. M. E. Williams (2009), The Stanislaus Table Mountain: Observations of a lava-capped inverted paleochannel for interpretation of inverted paleochannels on Mars, *Lunar Planet. Sci.*, *XL*, Abstract 1633.

Burr, D. M., J. P. Emery, R. D. Lorenz, G. C. Collins, and P. A. Carling (2006a), Sediment transport by liquid overland flow: Application to Titan, *Icarus*, *181*, 235–242, doi:10.1016/j.icarus.2005.11.012.

Burr, D. M., R. M. E. Williams, J. Nussbaumer, and J. R. Zimbelman (2006b), Multiple, distinct, (glacio?)fluvial paleochannels throughout the western Medusae Fossae Formation, Mars, *Lunar Planet. Sci.*, *XXXVII*, Abstract 1367.

Burr, D. M., M.-T. Enga, R. M. E. Williams, J. R. Zimbelman, A. D. Howard, and T. A. Brennand (2009), Pervasive aqueous paleoflow features in the Aeolis/Zephpyria Plana region, Mars, *Icarus*, *200*, 52–76, doi:10.1016/j.icarus.2008.10.014.

Carlston, C. A. (1965), The relation of free meander geometry to stream discharge and its geomorphic implications, *Am. J. Sci.*, *263*, 864–885.

Carr, M. H. (1996), *Water on Mars*, Oxford Univ. Press, New York.

Carter, L. M., et al. (2009), Shallow radar (SHARAD) sounding observations of the Medusae Fossae Formation, Mars, *Icarus*, *199*, 295–302, doi:10.1016/j.icarus.2008.10.007.

Christensen, P. R. (1982), Martian dust mantling and surface composition: Interpretation of thermophysical properties, *J. Geophys. Res.*, *87*(B12), 9985–9998, doi:10.1029/JB087iB12p09985.

Christensen, P. R., et al. (2003), Morphology and composition of the surface of Mars: Mars Odyssey THEMIS results, *Science*, *300*(5628), 2056–2061, doi:10.1126/science.1080885.

Ehlmann, B. L., et al. (2008), Orbital identification of carbonate-bearing rocks on Mars, *Science*, *322*(5909), 1828–1832, doi:10.1126/science.1164759.

Fassett, C. I., and J. W. Head (2005), Fluvial sedimentary deposits on Mars: Ancient deltas in a crater lake in the Nili Fossae region, *Geophys. Res. Lett.*, *32*, L14201, doi:10.1029/2005GL023456.

Fergason, R. L., P. R. Christensen, and H. H. Kieffer (2006), High-resolution thermal inertia derived from the Thermal Emission Imaging System (THEMIS): Thermal model and applications, *J. Geophys. Res.*, *111*, E12004, doi:10.1029/2006JE002735.

Greeley, R., N. T. Bridges, R. O. Kuzmin, and J. E. Laity (2002), Terrestrial analogs to wind-related features at the Viking and Pathfinder landing sites on Mars, *J. Geophys. Res.*, *107*(E1), 5005, doi:10.1029/2000JE001481.

Harris, D. R. (1980), Exhumed paleochannels in the Lower Cretaceous Cedar Mountain Formation near Green River, in *Brigham Young University Geology Studies*, vol. 27, pp. 51–66, Brigham Young Univ., Provo, Utah.

Hickin, E. J. (1974), The development of river meanders in natural river channels, *Am. J. Sci.*, *274*, 414–442.

Hynek, B. M., R. J. Phillips, and R. E. Arvidson (2003), Explosive volcanism in the Tharsis region: Global evidence in the Martian geologic record, *J. Geophys. Res.*, *108*(E9), 5111, doi:10.1029/2003JE002062.

Irwin, R. P., III, T. R. Watters, A. D. Howard, and J. R. Zimbelman (2004), Sedimentary resurfacing and fretted terrain development along the crustal dichotomy boundary, Aeolis Mensae, Mars, *J. Geophys. Res.*, *109*, E09011, doi:10.1029/2004JE002248.

Irwin, R. P., III, R. A. Craddock, and A. D. Howard (2005), Interior channels in Martian valley networks: Discharge and runoff production, *Geology*, *33*, 489–492, doi:10.1130/G21333.1.

Irwin, R. P., III, A. D. Howard, and R. A. Craddock (2008), Fluvial valley networks on Mars, in *River Confluences, Tributaries, and the Fluvial Network*, edited by S. Rice, A. Roy, and B. Rhoads, pp. 419–451, doi:10.1002/9780470760383.ch19, John Wiley, West Sussex, U. K.

Jones, S. J., and L. E. Frostick (2008), Inferring bedload transport from stratigraphic successions: Examples from Cenozoic and Pleistocene rivers, south central Pyrenees, Spain, in *Landscape Evolution: Denudation, Climate and Tectonics Over Different Time and Space Scales*, *Geol. Soc. London Spec. Publ. Ser.*, vol. 296, edited by K. Gallagher, S. J. Jones, and J. Wainwright, pp. 129–145, Geol. Soc. of London, London.

Kerber, L., and J. W. Head (2010), The age of the Medusae Fossae Formation: Evidence of Hesperian emplacement from crater morphology, stratigraphy, and ancient lava contacts, *Icarus*, *206*, 669–684, doi:10.1016/j.icarus.2009.10.001.

Kieffer, H. H., T. Z. Martin, A. R. Peterfreund, B. M. Jakosky, E. D. Miner, and F. Don Palluconi (1977), Thermal and albedo mapping of Mars during the Viking Primary Mission, *J. Geophys. Res.*, *82*(28), 4249–4291, doi:10.1029/JS082i028p04249.

King, N. M., J. W. Hillhouse, S. Gromme, B. P. Hausback, and C. J. Pluhar (2007), Stratigraphy, paleomagnetism, and anisotropy of magnetic susceptibility of the Miocene Stanislaus Group, central Sierra Nevada and Sweetwater Mountains, California and Nevada, *Geosphere*, *3*(6), 646–666, doi:10.1130/GES00132.1.

Kleinhans, M. G. (2005), Flow discharge and sediment transport models for estimating a minimum timescale of hydrological activity and channel and delat formation on Mars, *J. Geophys. Res.*, *110*, E12003, doi:10.1029/2005JE002521.

Knighton, D. (1998), *Fluvial Forms and Processes*, Arnold, London.

Komar, P. D. (1980), Modes of sediment transport in channelized water flows with ramifications to the erosion of the Martian outflow channels, *Icarus*, *42*, 317–329, doi:10.1016/0019-1035(80)90097-4.

Maizels, J. (1987), Plio-Pleistocene raised channel systems of the western Sharqiya (Wahiba), Oman, in *Desert Sediments—Ancient and Modern*, *Geol. Soc. London Spec. Publ. Ser.*, vol. 35, edited by L. Frostick and I. Reid, pp. 31–50, Geol. Soc. of London, London.

Malin, M. C., and K. S. Edgett (2001), Mars Global Surveyor Mars Orbiter Camera: Interplanetary cruise through primary mission, *J. Geophys. Res.*, *106*(E10), 23,429–23,570, doi:10.1029/2000JE001455.

Malin, M. C., et al. (2007), Context Camera Investigation on board the Mars Reconnaissance Orbiter, *J. Geophys. Res.*, *112*, E05S04, doi:10.1029/2006JE002808.

Mandt, K. E., S. L. de Silva, J. R. Zimbelman, and D. A. Crown (2008), The origin of the Medusae Fossae Formation, Mars: Insights from a synoptic approach, *J. Geophys. Res.*, *113*, E12011, doi:10.1029/2008JE003076.

Mandt, K. E., S. L. de Silva, J. R. Zimbelman, and D. Wyrick (2009), Distinct erosional progressions in the Medusae Fossae Formation, Mars, indicate contrasting environmental conditions, *Icarus*, *204*, 471–477, doi:10.1016/j.icarus.2009.06.031.

McEwen, A.S., et al. (2007), MRO's High Resolution Imaging Science Experiment (HiRISE), *J. Geophys. Res.*, *112*, E05S02, doi:10.1029/2005JE002605.

Mellon, M. T., B. M. Jakosky, and P. R. Christensen (2000), High-resolution thermal inertia mapping from the Mars Global Surveyor thermal emission spectrometer, *Icarus*, *148*, 437–455, doi:10.1006/icar.2000.6503.

Milazzo, M. P., et al. (2009), Discovery of columnar jointing on Mars, *Geology*, *37*, 171–174, doi:10.1130/G25187A.1.

Mills, H. H. (1981), Boulder deposits and the retreat of mountain slopes, or, "gully gravure" revisited, *J. Geol.*, *89*, 649–660, doi:10.1086/628628.

Mills, H. H. (1990), Thickness and character of regolith on mountain slopes in the vicinity of Mountain Lake, Virginia, as indicated by seismic refraction, and implications for hillslope evaluation, *Geomorphology*, *3*, 143–157, doi:10.1016/0169-555X(90)90042-O.

Moore, J. M., A. D. Howard, W. E. Dietrich, and P. M. Schenk (2003), Martian layered fluvial deposits: Implications for Noachian climate scenarios, *Geophys. Res. Lett.*, *30*(24), 2292, doi:10.1029/2003GL019002.

Niles, P. B., L. A. Leshin, and Y. Guam (2005), Microscale carbon isotope variability in ALH84001 carbonates and a discussion of possible formation environments, *Geochim. Cosmochim. Acta*, *69*(11), 2931–2944, doi:10.1016/j.gca.2004.12.012.

Osterkamp, W. R., and E. R. Hedman (1982), Perennial-streamflow characteristics related to channel geometry and sediment in Missouri River basin, *U.S. Geol. Surv. Prof. Pap.*, *1242*, 1–37.

Osterkamp, W. R., and T. J. Toy (1994), The healing of disturbed hillslopes by gully gravure, *Geol. Soc. Am. Bull.*, *106*, 1233–1241, doi:10.1130/0016-7606(1994)106<1233:THODHB>2.3.CO;2.

Pain, C. F., and C. D. Ollier (1995), Inversion of relief—A component of landscape evolution, *Geomorphology*, *12*, 151–165, doi:10.1016/0169-555X(94)00084-5.

Pain, C. F., J. D. A. Clarke, and M. Thomas (2007), Inversion of relief on Mars, *Icarus*, *190*, 478–491, doi:10.1016/j.icarus.2007.03.017.

Parker, G., P. R. Wilcock, C. Paola, W. E. Dietrich, and J. Pitlick (2007), Physical basis for quasi-universal relations describing bankfull hydraulic geometry of single-thread gravel bed rivers, *J. Geophys. Res.*, *112*, F04005, doi:10.1029/2006JF000549.

Putzig, N. E., and M. T. Mellon (2007), Apparent thermal inertia and the surface heterogeneity of Mars, *Icarus*, *191*, 68–94, doi:10.1016/j.icarus.2007.05.013.

Reid, L., J. C. Bathurst, P. A. Carling, E. E. Walling, and B. W. Webb (1997), Sediment erosion, transport and deposition, in *Applied Fluvial Geomorphology for River Engineering and Management*, edited by C. R. Thorne, R. D. Hey and M. D. Newsom, pp. 95–135, Wiley, Chichester, U. K.

Rhodes, D. D. (1980), Exhumed topography—A case study of the Stanislaus Table Mountain, California, *Natl. Aeronaut. Space Admin. Tech. Memo. 82385*, pp. 397–399, NASA Off. of Space Sci., Washington, D. C.

Rhodes, D. D. (1987), Table Mountain of Calaversa and Tuolumne counties, California, in *Centennial Field Guide*, vol. 1, *Cordilleran Section*, edited by M. L. Hill, pp. 269–272 Geol. Soc. of Am., Boulder, Colo.

Rodnight, H., G. A. T. Duller, S. Tooth, and A. G. Wintle (2005), Optical dating of a scroll-bar sequence on the Klip River, South Africa, to derive the lateral migration rate of a meander bend, *Holocene*, *15*(6), 802–811, doi:10.1191/0959683605hl854ra.

Ruff, S. W., and P. R. Christensen (2002), Bright and dark regions on Mars: Particle size and mineralogical characteristics based on Thermal Emission Spectrometer data, *J. Geophys. Res.*, *107*(E12), 5127, doi:10.1029/2001JE001580.

Scott, D. H., and K. L. Tanaka (1982), Ignimbrites of Amazonis Planitia region of Mars, *J. Geophys. Res.*, *87*(B2), 1179–1190, doi:10.1029/JB087iB02p01179.

Sparks, R. S. J. (1976), Grain-size variations in ignimbrites and implications for the transport of pyroclastic flows, *Sedimentology*, *23*, 147–188, doi:10.1111/j.1365-3091.1976.tb00045.x.

Taylor, J. R. (1982), *An Introduction to Error Analysis: The Study of Uncertainties in Physical Measurements*, Univ. Sci. Books, Sausalito, Calif.

Tooth, S., H. Rodnight, T. S. McCarthy, G. A. T. Duller, and A. T. Grundling (2009), Late Quaternary dynamics of a South African floodplain wetland and the implications for assessing recent human impacts, *Geomorphology*, *106*, 278–291, doi:10.1016/j.geomorph.2008.11.009.

Ward, A. W. (1979), Yardangs on Mars: Evidence of recent wind erosion, *J. Geophys. Res.*, *84*(B14), 8147–8166, doi:10.1029/JB084iB14p08147.

Wells, G. L., and J. R. Zimbelman (1997), Extraterrestrial arid surface processes, in *Arid Zone Geomorphology: Process, Forms and Change in Drylands*, 2nd ed., edited by D. S. G. Thomas, pp. 659–690, John Wiley, Chichester, U. K.

Wendell, K. D., D. M. Burr, R. M. E. Williams, and A. D. Howard (2008), Paleodischarge of inverted fluvial features in the Aeolis/Zephyria Plana, Mars, *Eos Trans. AGU*, *89*(53), Fall Meet. Suppl., Abstract P41A-1345.

Williams, G. P. (1983), Improper use of regression equations in Earth sciences, *Geology*, *11*(4), 195–197, doi:10.1130/0091-7613(1983)11<195:IUOREI>2.0.CO;2.

Williams, G. P. (1984), Paleohydrologic equations for rivers, in *Developments and Applications of Geomorphology*, edited by J. E. Costa and P. J. Fleisher, pp. 343–367, Springer, Berlin.

Williams, G. P. (1986), River meanders and channel size, *J. Hydrol.*, *88*, 147–164, doi:10.1016/0022-1694(86)90202-7.

Williams, G. P. (1988), Paleofluvial estimates from dimensions of former channels and meanders, in *Flood Geomorphology*, edited by V. R. Baker et al. pp. 321–334, Wiley, New York.

Williams, R. M. E., and R. P. Irwin III (2009) Morphology of lava-capped inverted valleys near St. George, Utah: Analogs for Martian sinuous ridges, *Lunar Planet. Sci.*, *XL*, Abstract 2413.

Williams, R. M. E., T. C. Chidsey, and D. E. Eby (2007) Exhumed paleochannels in central Utah–Analogs for raised curvilinear features on Mars, in *Central Utah–Diverse Geology of a Dynamic Landscape*, *Utah Geol. Assoc. Publ. Ser.*, vol. 36, edited by G. C. Willis et al., pp. 221–235, Utah Geol. Assoc., Salt Lake City.

Williams, R. M. E., R. P. Irwin, and J. R. Zimbelman (2009), Evaluation of paleohydrologic models for inverted channels: Applications to Mars, *Geomorphology*, *107*, 300–315, doi:10.1016/j.geomorph.2008.12.015.

Wilson, L., G. J. Ghatan, J. W. Head, and K. L. Mitchell (2004), Mars outflow channels: A reappraisal of the estimation of water flow velocities from water depths, regional slopes, and channel floor properties, *J. Geophys. Res.*, *109*, E09003, doi:10.1029/2004JE002281.

Zimbelman, J. R. (1986), The role of porosity in thermal inertia variations on basaltic lavas, *Icarus*, *68*, 366–369, doi:10.1016/0019-1035(86)90028-X.

D. M. Burr, M. Chojnacki, and J. P. Emery, Earth and Planetary Science Department, University of Tennessee Knoxville, 1412 Circle Dr., Knoxville, TN 37996-1410, USA. (dburr1@utk.edu)

R. M. E. Williams, Planetary Science Institute, 1700 E. Fort Lowell, Suite 106, Tucson, AZ 85719-2395, USA.